Effect of Manganese Promotion on the Activity and Selectivity of Cobalt Catalysts for CO Preferential Oxidation

Liping Zhong,[a], Mathias Barreau,[a,*] Dingkai Chen,[a] Valérie Caps,[a] Michael Haevecker,[b,c] Detre Teschner, [b,c] David H. Simonne,[d] Elisa Borfecchia,[d] Walid Baaziz,[e] Břetislav Šmíd,[f] and Spyridon Zafeiratos,[a,*]

[a]*Institut de Chimie et Procédés pour l'Energie, l'Environnement et la Santé (ICPEES), ECPM, UMR 7515 CNRS – Université de Strasbourg, 25 rue Becquerel, 67087 Strasbourg Cedex 02, France*

[b]*Max-Planck-Institut für Chemische Energiekonversion (MPI-CEC), Stiftstrasse 34-36, D-45470 Mülheim a.d. Ruhr, Germany*

[c]*Fritz-Haber-Institut der Max-Planck-Gesellschaft, Faradayweg 4-6, D-14195 Berlin, Germany*

[d]*Department of Chemistry, INSTM Reference Center and NIS Centers, University of Torino, Via P. Giuria 7, 10125 Torino, Italy*

[e]*Institut de Physique et Chimie des Matériaux de Strasbourg (IPCMS), UMR 7504 CNRS – Université de Strasbourg, 23 rue du Loess BP 43, 67034 Strasbourg cedex 2, France*

[f]*Charles University, Faculty of Mathematics and Physics, Department of Surface and Plasma Science, V Holešovičkách 2, 18000, Prague 8, Czech Republic*

Abstract

The preferential oxidation of CO in H_2-rich mixtures (COPrOx) is a major catalytic reaction utilized for hydrogen purification. In the exploration of alternatives to noble metals, cobalt-based catalysts appear to be a very promising choice. The activity and stability of cobalt in the COPrOx reaction can be improved by the addition of transition metals and manganese is maybe the most prominent among them. Yet, the arrangement of the two components in the catalytically active state is largely unknown, which hinders in-depth understanding of the manganese promotion effect. Here, we compare pure and Mn-modified cobalt catalysts and correlate their structural and chemical characteristics with their COPrOx performance. The Mn-promoted cobalt catalyst is significantly more active than pure cobalt especially at intermediate reaction temperatures (around 200 °C). The addition of Mn improves the structural stability of the catalyst and helps to maintain higher specific surface areas. Chemical and microstructural analysis using various *operando* and *in situ* techniques revealed that Mn promotes CO conversion by partially stabilizing CoO phase during reaction conditions. It is also suggested that at high temperature, Mn suppress CO methanation reaction but promotes H_2 oxidation. Apart of the particular interest in COPrOx reaction, in a general context, this work shows how the spatial distribution of the different

catalyst components at nanoscopic level, may affect the surface chemistry and consequently control the reactivity.

Keywords : COPrOx; cobalt oxides; manganese oxides; mixed oxides; selectivity; operando spectroscopy; NAP-XPS; NEXAFS

1 Introduction

CO preferential oxidation (COPrOx) is one of the most straightforward and efficient methods to eliminate CO from blue hydrogen-feed for subsequent utilization as fuel in proton-exchange membrane fuel cells (PEMFCs) [1–4]. An ideal COPrOx catalyst should be highly selective to CO oxidation but not to H_2 oxidation and CO methanation reactions [4]. Platinum group metals (Ru, Au, Pt, Pd) supported on various oxides can achieve 100% CO conversion in the hydrogen feed at relatively low temperature [5–9]. However, the high price and limited availability of noble materials have urged the development of COPrOx catalysts based on using abundant, thus economic viable, elements such as Cu, Ni andCo [10–13]. Among them, Cu oxides supported on CeO_2 have comparable performance to noble metal catalysts [14–18]. The excellent activity of CuO-CeO_2 system was attributed to the remarkable oxygen-storage/releasing capacity of ceria and the charge transfer between Cu^{2+}/Cu^{+} and Ce^{4+}/Ce^{3+} [19–21].

Besides copper, cobalt oxide catalysts are known to be active for CO oxidation especially at very low temperatures (down to -77 °C) [22]. Moreover, Co_3O_4 nanostructures with certain morphologies [23] or deposited on befitting supports, have displayed excellent activity for COPrOx [24–29]. Nevertheless, so far, the reported cobalt-based catalysts cannot meet the requirements for successful commercialization in COPrOx reaction. The high onset temperature of CO oxidation under COPrOx conditions, CO methanation at higher temperature and the fast deactivation of the catalyst are the main performance deficiencies [30]. In the search for a better catalysts it has been noticed that the reactivity and selectivity of cobalt can be improved by promotion with an additional oxide [31,32]. Among various oxides, MnO_x and CeO_2 additives/promoters have shown the most promising COPrOx catalytic performances [32–41].

Notably, several groups have reported that Mn surpasses other metal promoters and boosts cobalt performance for both CO oxidation [32–34,39,40,42–46] and COPrOx reactions [32,34,47]. The positive effect of manganese is not well understood, but some authors speculated that MnO_x contributes to the stabilization of Co^{3+} species at the surface by facilitating oxidation of Co^{2+} to Co^{3+} [32,40]. This hypothesis presumes that Co^{3+} sites of Co_3O_4 are the active sites for COPrOx which opposes recent findings about the negative role of Co_3O_4 in the activity [48,49]. This evident contradiction was a driving force to investigate in detail the promotional effect of Mn on Co for COPrOx.

Pure manganese oxides are active for CO oxidation [50], but there are no reports regarding their intrinsic activity as compared to that of cobalt oxides, neither about their selectivity in H_2-rich mixtures. Similar to cobalt, the reactivity of manganese oxides is affected by their oxidation state in the order: $MnO<MnO_2<Mn_2O_3$ at 250 °C [51,52]. This indicates that the oxidation state of manganese may be essential for CO conversion over Mn-Co catalyst. However, to the best of the

authors' knowledge the evolution of Mn oxidation state in Co-Mn system during the COPrOx has never been studied in detail. This provides an additional motivation for the study of Co-Mn using *in situ* surface sensitive methods.

In a more general context, understanding the interaction and the arrangement between the elements of a hybrid catalyst can help to obtain the desired reactivity by adjusting the composition and distribution of these elements [53]. The catalyst components may either form a single phase, for example a mixed oxide, or incorporate as a composite material where two or more distinct phases are arranged separately at microscopic level. In the latter case, different reactivity trends can be obtained depending on the variations of the composition, and the distribution, of the two metals/oxides forming the catalyst [8]. Comprehension of the catalyst's performance requires detailed information about the vertical and lateral distribution of the two components over a working catalyst. This type of information is typically retrieved from well-defined model catalytic systems [54], while in this regard realistic powder catalysts, synthesized by a standard chemical synthesis methods, remain poorly investigated. Accordingly, this study reports on the interaction between cobalt and manganese in powder catalysts, under COPrOx conditions. The aim is to describe the relation between the surface oxidation state and the resulting catalytic performance. Based on literature results, the Co:Mn = 1:0.125 mixing ratio seems to be optimal for COPrOx [34,47]. Therefore, in this work we did not try to optimize the Co-Mn catalyst composition, but we adopted the one reported (Co_8MnO_x) to have the best activity [34,47]. For comparison, two other unsupported catalysts (CoO_x and $CoMn_8O_x$) were prepared. In order to focus on the activity of cobalt oxides and circumvent the effects induced by the support, unsupported nanopowders were used. In addition to the *ex situ* structural and morphological characterization (H_2-TPR, XRD, ICP, SEM, BET, STEM-EDX, HRSTEM), X-ray spectroscopic techniques (NAP-XPS and NEXAFS), including both synchrotron and laboratory based-experiments, were used to investigate *in situ* the evolution of each component during COPrOx.

2 Materials and Methods

2.1 Catalysts preparation

Commercially available nanoparticulate cobalt monoxide (CoO, 99.99%, Sigma Aldrich CAS# 1307-96-6) was used as catalyst in its pure form (CoO_x), or as a support for the synthesis of the Co-Mn catalyst (Co_8MnO_x). The Co_8MnO_x catalyst was synthesized by incipient wetness impregnation. In details, 0.5025 g of Manganese (II) nitrate tetrahydrate ($Mn(NO_3)_2.4H_2O$) was dissolved in 0.317 g of water. The obtained solution was added to 1.2 g CoO and the obtained mixture was dried in air at 120 °C for 12 h. The dry product was subsequently calcined in air at 400 °C for 3 h. The same synthesis method was used for the preparation of the reference $CoMn_8O_x$ catalyst (the atomic ratio of Mn/Co was 8/1 in this case), however, in this case Mn_3O_4

acted as support and was impregnated with the cobalt-containing solution. In details, 1.83 g of commercial Mn_3O_4 (Sigma-Aldrich, 97%) was impregnated with an aqueous solution of 0.582 g of $Co(NO_3)_2.6H_2O$ (ACROS Organics, 99%) in 0.144 g of water. Then, the mixture was dried for 12 h at 120 °C and subsequently calcined in air at 400 °C for 3 h.

2.2 Catalytic tests

The catalytic oxidation of CO in the presence of H_2 was performed in a fully automated fixed-bed flow reactor (CETRIB SARL, Andlau, France) [49,55]. 50 mg of the catalytic powder was introduced in a quartz glass tube (i.d. 10 mm) and dispersed evenly on a P3 glass frit (16-40 μm). Average thickness of the catalytic bed was about 1 mm. The glass reactor was then introduced in a tubular oven with the catalyst bed located in the isothermal zone. Gas mixtures were generated using calibrated (Serv Instrumentation) mass flow controllers (Bronkhorst). The COPrOx gas mixture was composed of 1% CO, 1% O_2, 50% H_2 balanced in helium. The feed gas was introduced in the reactor at a total flow rate of 50 mL·min^{-1} (1 atm, GHSV ~ 7,500 h^{-1}). The temperature was monitored by a type K thermocouple plunged inside the catalytic bed. The reactants and products were monitored by a Compact Gas Chromatograph (CGC from Interscience, Belgium) equipped with a TCD detector. Detection and quantification of water was not possible since the products were filtered by a moisture trap before the introduction in the GC columns. The H_2 conversion, which is very low, was not quantified due to the low TCD sensitivity in H_2 variations when using He as carrier gas. Prior to each test, the catalysts were reduced *in situ,* by using the following protocol: heating at 400 °C for 30 min in 100% H_2 (50 mL·min^{-1}) with a heating rate of 10 °C·min^{-1} and cooling back down to 30 °C. The residual oxygen content of the gas phase was below 100 ppm. Although not standard in COPrOx studies, the pre-reduction step was needed for better consistency with the procedure followed in the spectroscopic studies described below. For light-off tests, the catalyst was heated under the COPrOx mixture to 50, 100, 150, 200, 250, 300 and 350 °C using a ramp of 10 °C·min^{-1} and dwell time of 30 min at each temperature. Short-term stability tests were conducted for about 5 h at 250 and 300 °C. Stability tests were performed after light-off tests using the same sample, but pre-reduced in H_2 at 400 °C to assure the same initial oxidation state of catalysts in stability and light-off tests. The CO and O_2 (X_{CO}, X_{O2}) conversions, the O_2 to CO_2 selectivity (S_{CO2}), the CH_4 selectivity (S_{CH4}) as well as the CO_2 and CH_4 yields (Y_{CO2} and Y_{CH4}) were calculated as follows:

CO conversion: $X_{CO}(\%) = \frac{CO_{in} - CO_{out}}{CO_{in}} \times 100$ Equation (1)

O_2 Conversion: $X_{O2}(\%) = \frac{O_{2,in} - O_{2,out}}{O_{2,in}} \times 100$ Equation (2)

CO_2 selectivity: $S_{CO2}(\%) = \frac{CO_{in} - CO_{out}}{2(O_{2,in} - O_{2,out})} \times 100$ Equation (3)

CH_4 Selectivity: $S_{CH4}(\%) = \frac{CH_{4,out}}{CO_{in}-CO_{out}} \times 100$ Equation (4)

CO_2 Yield : $Y_{CO2}(\%) = \frac{CO_{2,out}}{CO_{out}+CO_{2,out}+CH_{4,out}} \times 100$ Equation (5)

CH_4 Yield : $Y_{CH4}(\%) = \frac{CH_{4,out}}{CO_{out}+CO_{2,out}+CH_{4,out}} \times 100$ Equation (6)

where: $CO_{out/in}$, $O_{2,out/in}$, $CO_{2,out}$ and $CH_{4,out}$ are the concentrations at in/outlet of the reactor at each reaction temperature. The concentration of each gas is quantified by GC peak area multiplication with the response factor of each gas determined by external calibration. Note that in the case of CH_4 formation Eq. 3 overestimates the S_{CO2}, since CH_4 and CO_2 are not directly included in the calculations. Therefore the S_{CO2} should be consulted in combination with Eq. 4 and 6.

2.3 Structural and morphological characterization

Temperature-programmed reduction (H_2-TPR) profiles were recorded in an automated catalyst characterization system (Micromeritics, model AutoChem II), which incorporates a thermal conductivity detector (TCD). 50 mg of the sample was loaded in a U tube and heated by 5 °C·min^{-1} under 10 mL·min^{-1} of 10% H_2 in Ar. Elemental analysis of the calcined Co-Mn based materials was performed by Inductively Coupled Plasma Optical Emission Spectroscopy (ICP-OES, Varian 720ES) after dissolution of the powdered sample in acidic medium followed by filtration of residual particles. *Ex situ* XRD patterns were collected on a Bruker D8 advance diffractometer using Cu Kα radiation. The crystallite size of the reduced and spent catalysts was calculated using the Scherrer's equation [56]. For the Co^0 hcp (JCPDS 05-0727) and fcc (JCPDS 15-0806) phases, they were determined according to the line broadening of the (100) and (200) plans located at 41.8 and 51.6°, respectively. For the MnO phase (JCPDS 07-0230), the reflection at 40.9° corresponding to the (200) plan was used for the calculation. The BET specific surface area of Co-Mn based materials was determined by N_2 physisorption measurements, while Kr-BET was used for pure CoO for higher precision measurements due to the extremely low surface area. Samples were degassed at 200 °C for 5 h before launching the adsorption-desorption of N_2. The specific surface areas were calculated according to the Brunauer–Emmett–Teller (BET) method using data points in the relative pressure (p/p0) range of 0.05–0.35. The N_2-BET measurements were repeated twice with similar results (±10%). Scanning Transmission electron microscopy (STEM) analysis of calcined, reduced and spent $CoMn_8O_x$ catalysts was carried out using a JEOL 2100 FEG S/TEM microscope operated at 200 kV equipped with a spherical aberration corrector on the probe forming lens. The samples were dispersed by ultrasonication in ethanol and deposited on holey carbon coated TEM grid. The STEM images were carried out using a spot size of 0.13 nm, a current density of 140 pA and a camera focal length of 8 cm,

corresponding to the inner and outer diameters of the annular detector of about 73 and 194 mrad. Elemental analyses of Co, Mn and O were carried out with an EDX probe using a silicon drift detector (SDD) with a sensor size of 60 mm^2. The morphology of fresh and spent catalysts was examined by a Zeiss GeminiSEM 500 SEM microscope, combining with energy dispersive X-ray spectroscopy (EDX) to study the distribution of elements on surface.

2.4 Synchrotron-based *in situ* spectroscopic study

Synchrotron-based *in situ* NAP-XPS and NEXAFS experiments were performed at CAT branch of the EMIL beamlines (Energie Materials In-situ Laboratory Berlin) at the synchrotron radiation facility BESSY II of the Helmholtz Zentrum Berlin [57,58]. Two catalysts (pure CoO_x and Co_8MnO_x) were examined under identical conditions on a comparative basis. The powder catalysts were pressed into pellets and mounted on the sample holder using a stainless-steel mask. The sample stage was heated from the back side by an IR laser and the temperature was measured by a K-type thermocouple attached to the sample surface. The gases were introduced in the analysis chamber (about 10 L volume) *via* four calibrated mass flow controllers (Bronkhorst) and the total flow rate was kept constant at 15 $mL \cdot min^{-1}$. The COPrOx mixture composition was: 1% CO, 1% O_2 and 50% H_2 in He and the total pressure was kept at 0.5 mbar. The gas phase composition was monitored by a differentially pumped quadrupole mass spectrometer (QMS, Pfeiffer PrismaPro), which was connected to the experimental cell through a leak valve. Unfortunately, the gas phase signal changes during reaction were minor and unfit for analysis. The entrance of the electron analyzer lenses was of cone-shape (nozzle) ending with a 1 mm diameter hole. The sample/nozzle distance during NAP-XPS measurements was kept around 2 mm. The Co 2p and Mn 2p spectra were recorded using specific photon energies, so that the collected photoelectrons to have the same kinetic energy (240 or 560 eV) allowing similar sample information depths (ca. 2 and 3.5 nm, respectively). The NEXAFS Co L_3-edge and Mn L_3-edge peaks were measured in the total electron yield (TEY) mode. Given the possibility that Mn oxides might be reduced by the synchrotron radiation, Mn 2p spectra have been recorded twice at different time spans of the experiment. The similarity of the spectra suggests that the oxidation state of Mn is not affected by the continuous exposure to the X-ray beam.

2.5 Operando NAP-XPS study using a monochromatic AlKα X-ray source

The *operando* NAP-XPS study of pure CoO_x, Co_8MnO_x and $CoMn_8O_x$ catalysts was performed at Charles University in Prague, Czech Republic. The experiments were carried out on a photoelectron spectrometer (SPECS Surface Nano Analysis GmbH, Germany) which is equipped with a PHOIBOS-150 multichannel hemispherical electron energy analyzer coupled with a differentially pumped electrostatic pre-lens system. Spectra were obtained using the monochromatized Al Kα X-ray source (1486.6 eV). The powder of fresh as-synthesized catalysts

was pressed to pellets and fixed on the sample holder using a stainless-steel mask with a window at the top. The thermocouple was welded on the mask at the side which was in contact with the sample surface. The reactor cell volume was 0.4 L and the catalyst was investigated in 1.3 mL·min^{-1} flow of pure H_2, pure O_2 and in a COPrOx feed with the $CO:O_2:H_2$ molar ratios of 1:1:98 (note, He was not co-fed in this experiment). Before introduction of the COPrOx gases, the sample was pre-reduced in 1 mbar H_2 at 400 °C for about 2 h. After cooling down to 50 °C, the COPrOx mixture was introduced into the NAP-XPS cell and the pressure stabilized to 1 mbar. The XPS spectra were collected after 30 min in each temperature. Similar to synchrotron-based NAP-XPS the entrance of the photoelectrons to the lenses was via a nozzle, but in this case the entrance hole diameter was much smaller (0.3 mm) which allows a distance between sample and nozzle of the same value. The gas phase in the cell was monitored by a QMS (Pfeiffer PrismaPro) fitted in the 1st pumping stage of the analyzer pre-lenses. Details about the conversion and selectivity calculation method by using the QMS signals can be found in supporting information 1.

2.6 In situ NEXAFS at 1bar under model redox conditions

The Co_8MnO_x sample was analyzed in 1 bar of H_2 and O_2 by NEXAFS at the APE-HE beamline of the Elettra synchrotron radiation facility (Trieste, Italy), using a dedicated reaction cell described in detail elsewhere [59]. The NEXAFS signal was detected in TEY mode, by probing the drain current from the sample with a picoammeter. The gases were introduced in the reaction cell via calibrated mass flow controllers keeping a constant gas flow of 50 mL·min^{-1}. Initially the sample was treated in O_2 at 200 °C for 15 min and subsequently cooled down under He gas flow. In situ NEXAFS spectra at Co and Mn L_3-edges were recorded at selected temperatures in the 38-250 °C range first in 100% H_2 and then in 10% O_2/He. NEXAFS data were acquired after 15 min at each selected temperature point. Data treatment, involving energy alignment, background subtraction using an asymmetric least square fitting routine and normalization to the total area under the curves, was performed by using the recently developed THORONDOR code [60]. The relative concentration of each oxidation state was calculated based on linear combination fit (LCF) analysis using as reference NEXAFS spectra of model Co and Mn oxides obtained from previous experiments [48] or from the literature [61]. LCF was carried out using the ATHENA program [62], for the experimental *in situ* NEXAFS data at Co and Mn L_3-edge, pretreated in THORONDOR. LCF errors on the retrieved relative fractions of each component are estimated to be ±5%.

2.7 Uncertainties in the comparison of spectroscopic results between different setups

This paper discusses *in situ*/operando spectroscopic results collected in 3 different spectrometers. Evidently the analysis chamber of the spectrometer also serves as a catalytic cell in this case. As described above the design of each setup is quite distinct, likely influencing the reaction conditions in each experiment. One can mention here the difference in the cell volume,

possible offset in the temperature reading due to the positioning of the thermocouple or the type of heating (laser or resistive heater), the flow of the reactants and their dilution, or not, in He. All these differences complicate the comparison of the results between different spectrometers and can explain for example the relatively stable CoO phase in the laboratory NAP-XPS tests as will be shown below. Notably, the COPrOx reactants flow has a clear effect on the reactivity and the surface oxidation state of cobalt as will be discussed in a future publication [63]. One should note that the QMS signal response in the laboratory-based NAP-XPS experiment was better as compared to the synchrotron-based NAP-XPS described above. Since the two setups use the same QMS, the reason behind this difference is most likely related to the particular reaction conditions applied in the two NAP-XPS spectrometers. These include the pressure (0.5 against 1 mbar), the contact time between the catalyst and the gas phase (linked with the setup design, the volume of the reactor/cell (10 vs. 0.4 L), the size of the pellet, the flow rate (15 vs. 1.3 $mL \cdot min^{-1}$), *etc.*) and definitely the installation position of the QMS in the two instruments.

2.8 Peak fitting and quantitative analysis of XPS spectra

The Co 2p spectra were fitted using standard reference curves of metallic Co, CoO and Co_3O_4 recorded at the same spectrometer. The full width at the half maximum and the energy difference between the three reference peaks were fixed for the fitting. The reference peaks were allowed to vary until the difference between their sum and the experimental spectra (residual standard deviation, STD) was minimized (typically between 1 and 2). The procedure was repeated twice using different initial and final background positions as well as, linear and spline-linear backgrounds (this is justified since reference peaks and spectra recorded on the catalysts do not necessarily have the same background profiles). The error bars in the quantification of the different cobalt oxidation states shown in the bar-graphs below represent the STD of the two fitting approaches by the mean value. The deconvolution of the Mn 2p peak is more challenging owing to the similarities of the various peaks corresponding to each Mn phase. However, by superimposing two Mn 2p spectra small differences were distinguished due to the divergence in the peak position and width (of about 0.2-0.3 eV) of the various manganese oxidation states. To enhance the robustness of the peak fitting procedure, four different approaches were used for Mn 2p peak deconvolution. These fitting approaches involved peak profiles of reference Mn components or using 6 individual Gaussian/Lorentzian (GL) peaks, as well as different types of background subtraction (linear or Shirley type) [64]. The Mn oxidation state given in this paper is the mean value of the four deconvolution processes and the error bar corresponds to the maximum deviation among the four approaches. The Mn 2p profile between synchrotron, and laboratory-based NAP-XPS setups, was very similar (see figure S2) which validates the utilization of the same deconvolution procedure of the Mn 2p spectra in the two experiments. In this way, any error in the estimation of the relative amount of the Mn^{2+}, Mn^{3+} and Mn^{4+} should be

systematic and consistent throughout this study. Quantitative analysis of elements was performed using normalized intensities and, for synchrotron-based photoemission studies, the photon flux and energy dependence of the atomic subshell photoionization cross sections [65] were taken into account. The XPS Co 2p and Mn 2p peak intensities were simulated using SESSA vs.2.1.1 software [66] for model consisting of MnO_2 particles supported on planar CoO substrate. Three MnO_2 particle morphologies (cubes, hemispheres and regular pyramids with square base) and five particle sizes (from 1.5 nm to 0.5 μm height) were modelled. The density of the particles on the support was left to vary up to the point where the simulated Co 2p and Mn 2p peak area ratio converged with the experimental one.

3 Results

3.1 Textural and morphological properties of CoO_x/MnO_x

The X-ray diffraction patterns of fresh (after calcination), reduced and spent catalysts are presented in figure S3. The pattern of fresh CoO_x corresponds to the single CoO phase (JCPDS 03-065-2902), but after reduction two types of metallic cobalt phases were found. The stronger diffraction peaks come from the face-centred cubic phase (fcc; JCPDS 15-0806) and the weaker from the hexagonal phase (hcp; JCPDS 05-0727) [67]. As far as the calcined Co_8MnO_x is concerned, all the observed peaks are attributed to Co_3O_4 (JCPDS 03-065-3103), without any trace of Mn-containing phases. The absence of Mn-related peaks might be due to low crystallinity and high dispersion of Mn. However, after reduction, small amounts of MnO are seen in the diffraction patterns, in addition to metallic cobalt. On the fresh $CoMn_8O_x$ sample, Co_3O_4-like phases are not observed and the most intense peaks are characteristic of a hausmannite phase (Mn_3O_4, JCPDS 01-089-4837) while small peaks indicate the presence of ramsdellite (MnO_2, JCPDS 01-073-1539). After reduction, only characteristic peaks of the MnO phase (JCPDS 07-0230) are detected implying reduction of MnO_2 and Mn_3O_4. The diffraction patterns of the spent catalysts remain almost identical with those after reduction, although a small increase in the crystalline size, probably due to sintering can be noticed. This indicates that the bulk structure of the catalysts does not change considerably during COPrOx reaction as compared to the H_2 pretreatment state.

The specific surface areas measured after the reduction pretreatment is shown in Table 1. The CoO_x catalyst has the lowest surface area of 1.4 m^2g^{-1} (measured by Kr-BET), while in case of Co_8MnO_x and $CoMn_8O_x$ the surface area is 6.5 and 8.5 $m^2\ g^{-1}$, respectively. The crystallite size estimated from the XRD patterns based on Scherrer's equation is included in the same table. The smaller crystallite size of Co^0 in Co_8MnO_x samples (please note that the same CoO_x particles were also used for Co_8MnO_x synthesis) suggests that the growth of metallic cobalt nanoparticles is prevented by the addition of Mn. The higher specific surface area of Co_8MnO_x (as compared with

CoO_x) is attributed to the presence of manganese oxide, since in general oxide phases have higher BET surface area than metals. ICP-OES was carried out to determine the Mn/Co content for each Co_8MnO_x and $CoMn_8O_x$ catalysts. The elemental analysis shown in Table 1 confirms that the bulk composition approximate very much the nominal one.

Table 1. Textural parameters of the catalysts.

Catalyst	*Mn/Co [a] Atomic ratio*	*S_{BET} (m^2 g^{-1})*	*Crystallite size[b] (nm)*	
	Calcined	*Reduced*	*Reduced*	*Spent*
CoO_x	0	1.4[c]	25.7 (Co^0 fcc), 24.4(Co^0 hcp)	34.7(Co^0 fcc), 34.4(Co^0 hcp)
Co_8MnO_x	0.10	6.5[d]	14.4 (Co^0 fcc), 24.3(Co^0 hcp), 23.2 (MnO)	19.1 (Co^0 fcc), 24.5(Co^0 hcp)
$CoMn_8O_x$	8.31	8.5[d]	23.0 (MnO)	23.8 (MnO)

a. The Mn/Co atomic ratio was determined by ICP-OES analysis *b*. The crystallite size of each major phase was estimated from the Scherrer's equation applied to the (100) plane of Co^0 hcp at 41.8°, the (200) plane of Co^0 fcc at 51.6° and the (200) plane of MnO at 40.9°*c* measured by Kr-BET *d* measured by N_2-BET.

H_2-TPR measurements were conducted with the aim to compare the bulk reducibility. As shown in figure S4 for the calcined pure CoO_x sample two main peaks are observed: one relatively sharp at 275 °C and a broader one centered around 365 °C. The two peaks are usually attributed to the progressive reduction of Co_3O_4 *via* a two-step process ($Co_3O_4 \rightarrow CoO \rightarrow Co$) [48]. The TPR profile of the Mn-rich catalyst ($CoMn_8O_x$) is dominated by peaks related to the progressive reduction of manganese oxide ($MnO_2 \rightarrow Mn_3O_4 \rightarrow MnO$) in accordance with literature reports [51,68]. In particular, the peaks at 270 °C and 440 °C correspond to MnO_2 and Mn_3O_4 reduction, respectively. Note that the reduction peaks of cobalt oxides are not clearly distinguished in this sample due to the relatively low amount of cobalt and the strong overlapping with the manganese oxides peaks. However, a broad peak is observed in the high temperature region (near 550 °C) which is not due to MnO_x or CoO_x and may be caused by synergetic interactions between Mn and Co species. In the TPR profile of the Co_8MnO_x catalyst a clear shift of the reduction peaks to the high-temperature region is found as compared to CoO_x. Similar shifts has been previously attributed to $Co_{3-x}Mn_xO_4$-type solid solution formed upon calcination [68–71], as expected according to the phase diagram of Co-Mn-O system [72] and experimental studies [73–75]. To examine the possibility of Co-Mn mixed oxide formation in the Co_8MnO_x catalyst we compared the XRD patterns of CoO_x and Co_8MnO_x samples after calcination. Typically, substitution of Co by Mn in Co_3O_4 structure, should shift the XRD peaks as compared to the pure Co_3O_4 phase, but in our case there was no evident shift between the Co_3O_4-related XRD peaks of the two catalysts suggesting that mixed Co-Mn-O phases either do not form at all in our

case, or are structurally disordered or nanosized and not detected by XRD.

The morphology of CoO_x, Co_8MnO_x and $CoMn_8O_x$ catalysts after calcination and reduction pretreatment was examined by SEM (figure S5). All three catalysts form big aggregates which are composed of fine particles clearly distinguished in most of the SEM micrographs. The particle size of CoO_x and Co_8MnO_x range between 50 and 200 nm, while in the case of $CoMn_8O_x$ (figure S5c) the particles seem even larger. After reduction at 400 °C, the particle size of both catalysts significantly increased. The images recorded after reduction of Co_8MnO_x clearly evidence a sintering process, with rougher surface as compared to its previous form. The EDX analysis of large surface areas of the Co_8MnO_x catalyst after calcination gave a Mn/Co ratio of around 1/10 (figure S6), which is close to the nominal value (0.125). Similar Mn/Co ratios were also found after analysis of individual spots on the surface, indicating that initially Mn is homogenously distributed over the cobalt surface. Interestingly, after the reduction pretreatment the EDX analysis of several spots revealed important differences in the Mn/Co ratios, which vary from 0.11 to 0.70, depending on the analysis spot. In addition, the spots with high Mn/Co ratios are always accompanied by high oxygen content.

Details about the microstructure of Co_8MnO_x catalyst were acquired by STEM combined with EDX analysis. STEM-EDX maps of several aggregates after H_2 pretreatment and COPrOx reaction (spent catalyst) are presented in figure 1a and b, while those of the fresh-calcined catalyst can be found in figure S7. The red and green colored areas in the figure indicate Co- and Mn-enriched areas, respectively. Elemental mapping confirms the significant inhomogeneity of the grains after reduction, shown above by SEM-EDX in larger scale, which is preserved without large variations also in the spent catalyst. In particular, in some sample areas Mn is well dispersed over Co particles, while in others Mn and Co areas are clearly separated. A common feature which is visible in several of the STEM-EDX images in figure 1 is that Mn content is increasing at the edge of the aggregates, suggesting that Mn is enriched on the surface of the grains. However, several other areas also exist where Co signal extends up to the perimeter of the aggregate revealing coexistence of uncovered/exposed cobalt surface. The % Mn and Co atomic concentration calculated from the EDX signal is included as pie charts in figure 1. The large variation of %Mn from 5 to 17% between the various micrographs evokes that Mn is not equally distributed over cobalt, but it is segregated and forms Mn-rich areas on the surface.

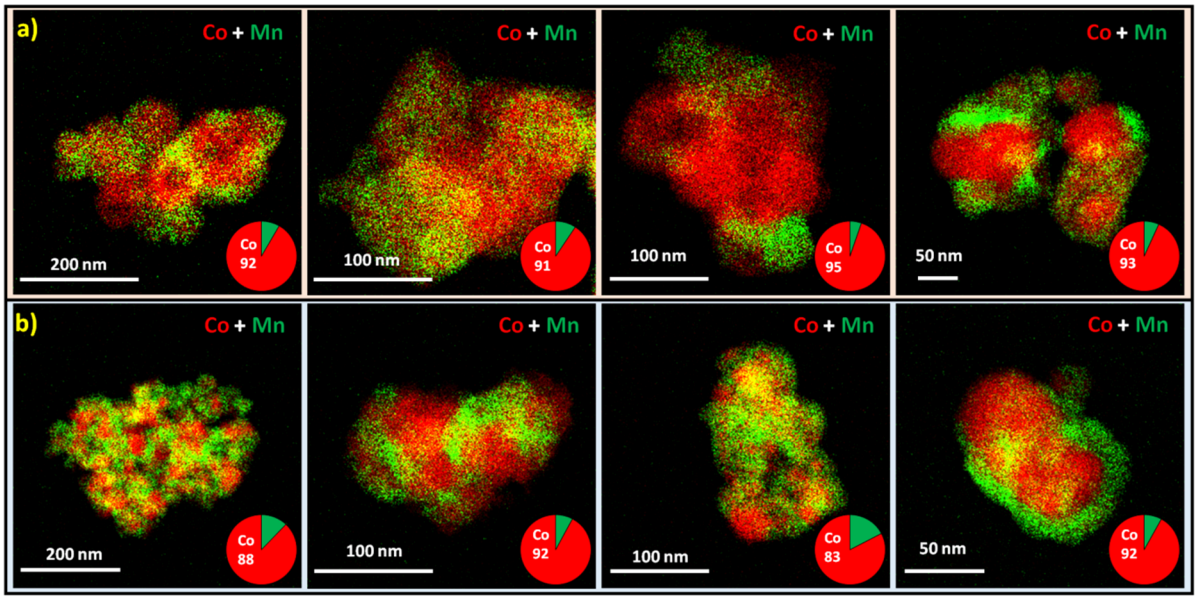

Figure 1. STEM-EDX analysis images with elemental mapping (merged Co+Mn) collected over several Co_8MnO_x catalyst aggregates after a) reduction at 400 °C in 1 bar H_2 for 30 min and b) spent catalyst after 6h reaction in 1 bar COPrOx at temperatures up to 350 °C. Red and green color areas correspond to Co- and Mn-enriched areas, respectively. The % atomic concentration of Mn and Co is presented in the pie charts at the right-bottom side of each panel.

3.2 Fixed-bed reactor catalytic tests

The reactivity of the three catalysts after H_2 reducing pretreatment was evaluated in a fixed-bed flow reactor. The CO conversion to CO_2 and CH_4 (X_{CO}) starts at 150 °C and increases sharply above this temperature for all catalysts (figure 2a), with the Co_8MnO_x having systematically higher X_{CO} than the other two. The differences are quite remarkable at intermediate temperatures, with more than 98% of CO conversion over Co_8MnO_x at 250 °C and only 51 and 29% for pure CoO_x and $CoMn_8O_x$, respectively. A small decrease from 98% to 96% of X_{CO} is observed for Co_8MnO_x above 250 °C. The O_2 conversion (X_{O2}) is the overall consumption of O_2 for both CO and H_2 oxidation (reaction 1 and 2, respectively). Please note here, that since the catalysts were pretreated in a reducing environment prior to the reaction, O_2 may also have been consumed to oxidize the pre-reduced cobalt, in addition to reaction 1 and 2. As shown in figure 2b, at 200 °C the Co_8MnO_x catalyst converts more O_2 than the other two but above this temperature the X_{O2} is stable at 95% for all catalysts.

The selectivity towards CO_2 (S_{CO2}, figure 2c) is similar for Co_8MnO_x and CoO_x up to 200 °C, but above this temperature Co_8MnO_x seems to be more selective than CoO_x. The $CoMn_8O_x$ catalyst has significantly lower S_{CO2} than the other two, which means that excess Mn promotes H_2 oxidation (reaction 2). However, since the S_{CO2} is determined on the basis of the CO amount consumed to form CO_2 and CH_4, comparison of the S_{CO2} above 250 °C is complicated due to CH_4 production. In this case the % CH_4 and CO_2 yields (Y_{CH4} and Y_{CO2} , respectively), shown in figure 2e and 2f, can help to distinguish differences in the carbon product selectivity among the catalysts. Indeed, the

CO_2 production over Co_8MnO_x and CoO_x reaches a maximum at 200 °C, while above this temperature CH_4 production is favored. In the case of $CoMn_8O_x$ the CO_2 yield increases constantly with temperature since CH_4 production is less favored on this catalyst. This behavior is also reflected in figure 2d where the selectivity of CO to CH_4 (S_{CH4}) increases significantly at 250 °C for all catalysts, showing that at this temperature CO hydrogenation (reaction 3) is promoted. The CH_4 production path via CO_2 hydrogenation (reaction 4) cannot be excluded completely, but it is less probable since CO is more easily hydrogenated than CO_2 under the same reaction conditions [76]. Please note that the S_{CH4} and S_{CO2} selectivities do not add up to 100% because they are based on independent CO and O_2 balances, respectively (see the denominators in eq. 3 and 4).

CO oxidation: $CO + ½\ O_2 \rightarrow CO_2$ (reaction 1)

H_2 oxidation: $H_2 + ½\ O_2 \rightarrow H_2O$ (reaction 2)

CO hydrogenation: $CO + 3\ H_2 \rightarrow CH_4 + H_2O$ (reaction 3)

CO_2 hydrogenation: $CO_2 + 4\ H_2 \rightarrow CH_4 + 2\ H_2O$ (reaction 4)

The stability tests shown in figure S8 confirm the results of the light-off tests, with Co_8MnO_x catalyst being the most active of all, with almost 2 times higher X_{CO} than CoO_x at 250 °C. There is a gradual decrease in the performance of the 3 catalysts with time as shown in Table S1. The Co_8MnO_x catalyst is more stable than the other two with around 4% X_{CO} loss per hour on stream, as compared to 10 and 22 % for CoO_x and $CoMn_8O_x$, respectively. The activity is recovered at 300 °C while the stability of all catalysts at this temperature seems to be improved.

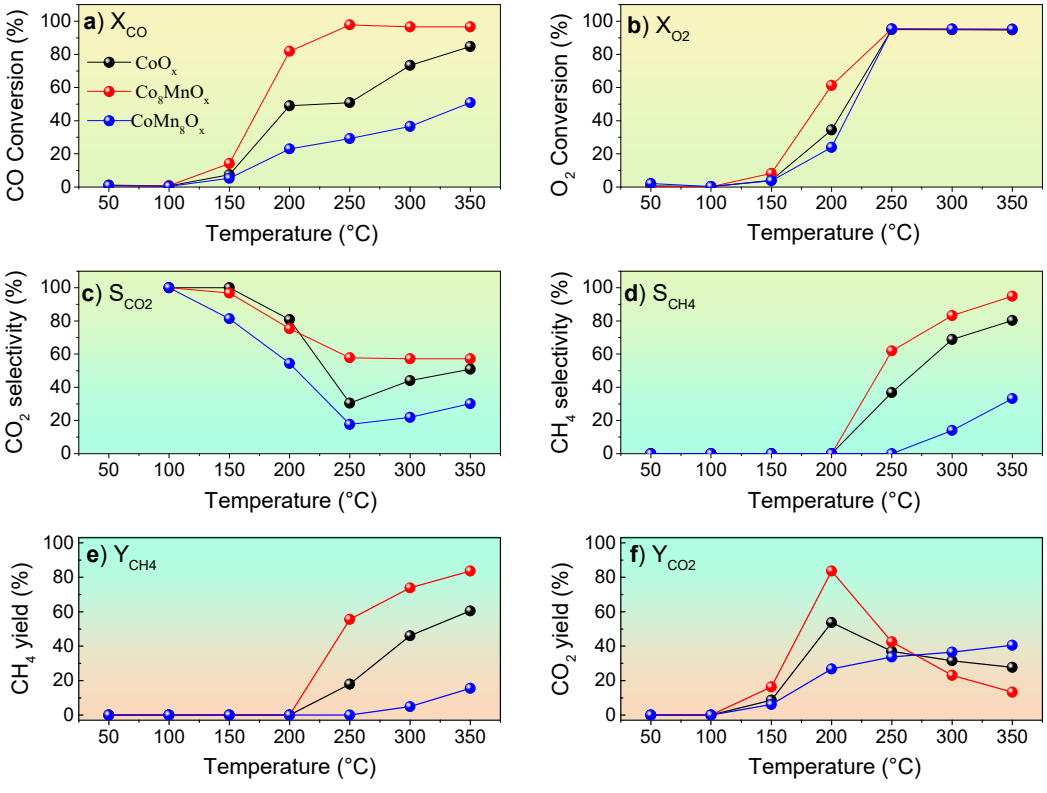

Figure 2. Fixed-bed reactor COPrOx activity tests : a) CO conversion, b) O_2 conversion,c) O_2 selectivity d) CH_4 selectivity, e) CH_4 yield and f) CO_2 yield *vs.* temperature, over pure CoO_x (●), Co_8MnO_x (●) and $CoMn_8O_x$ (●) catalysts. Experimental conditions: 1% CO, 1% O_2, and 50% H_2 in He-balanced flow; 0.05 g of catalyst; 50 mL min^{-1} of total flow; atmospheric pressure (1 bar). Every data point was recorded after 30 min equilibration at each temperature.

3.3 In situ surface characterization of the Co-Mn by *synchrotron* NAP-XPS and NEXAFS

The catalytic results suggest that addition of small amounts of Mn on CoO improves the activity and the selectivity towards CO_2, but excess of Mn (i.e. in the $CoMn_8O_x$ catalyst) is detrimental for the COPrOx reaction. In this paragraph *in situ* NAP-XPS and NEXAFS are used to compare the Co_8MnO_x and CoO_x surface oxidation state and composition under reaction conditions. The Co_8MnO_x catalyst was selected due to its superior performance as compared to $CoMn_8O_x$. The reactants feed composition, in the synchrotron-based NAP-XPS and NEXAFS experiment, was identical to the fixed-bed reactor tests, while relatively high reactant flows were used. The differences and similarities in the surface state of the two catalysts' observed by these methods are used to explain qualitatively their performance in the fixed-bed reactor.

3.3.1 Comparison of the cobalt oxidation state between the two catalysts

figure 3a displays the Co $2p_{3/2}$ spectra recorded on pure CoO_x after H_2 pretreatment and during the COPrOx reaction. Metallic cobalt (Co^0) formed in H_2, undergoes progressive oxidation during COPrOx reaction. The evolution of cobalt oxidation state was calculated by deconvolution of the Co 2p peak using reference spectra and it is presented in figure 3e. Just after 250 °C, metallic Co oxidize to CoO and in time undergoes further oxidation to Co_3O_4 stabilizing to a mixed Co_3O_4/CoO=65/35 state. The Co L_3-edge NEXAFS recorded after 1 h and 2 h at 250 °C under COPrOx conditions are shown together with reference CoO and Co_3O_4 spectra (in green dotted line) [77] in figure 3b. During COPrOx the Co L_3-edge has a maximum at 780.5 eV and a shoulder located at 778.5 eV, resembling the Co_3O_4 reference spectrum. However, the intensity ratio between the 780.5 eV and 778.5 eV peaks is different in the two cases. This difference, together with the small peak feature at 777.5 eV, marks the presence of cubic rocksalt CoO with Co^{2+} in octahedral position (O_h, see the reference in green dotted line) [48]. Consequently, both NAP-XPS and NEXAFS spectra of pure CoO_x catalyst suggest coexistence of Co_3O_4 and CoO species in COPrOx at 250 °C.

In case of the Co_8MnO_x the Co $2p_{3/2}$ peaks (figure 3c) and the cobalt oxidation state estimated from peak fitting, shown in figure 3f, indicate differences from CoO_x. In particular, after the H_2 pretreatment the catalyst is not totally reduced, and in general the Co_8MnO_x catalyst contains relatively more CoO. For example at 250 °C, CoO is about 46% in Co_8MnO_x after 1 h COPrOx while for CoO_x catalyst is only 35% at the same conditions. Similar conclusions can be also drawn from the NEXAFS spectra shown in figure 3d. The surface stability of Co_8MnO_x catalyst was examined at higher temperature than that of CoO_x, up to 350 °C. As shown in figure 3c, after 30 min at 350

°C metallic Co reappears at the expense of Co_3O_4, confirming previous reports about partial reduction of oxidized cobalt crystallites to metallic Co at higher COPrOx reaction temperatures [78]. However, longer reaction times (about 1 h at 350 °C) favor progressive re-oxidation to Co_3O_4. Surprisingly, the amount of CoO is not considerably influenced by the raise in the temperature and remains around 50% at both temperatures. At 350 °C the Co L_3-edge peak shape is modified as compared to 250 °C indicating a mixture of Co-CoO-Co_3O_4, in full accordance with the NAP-XPS results.

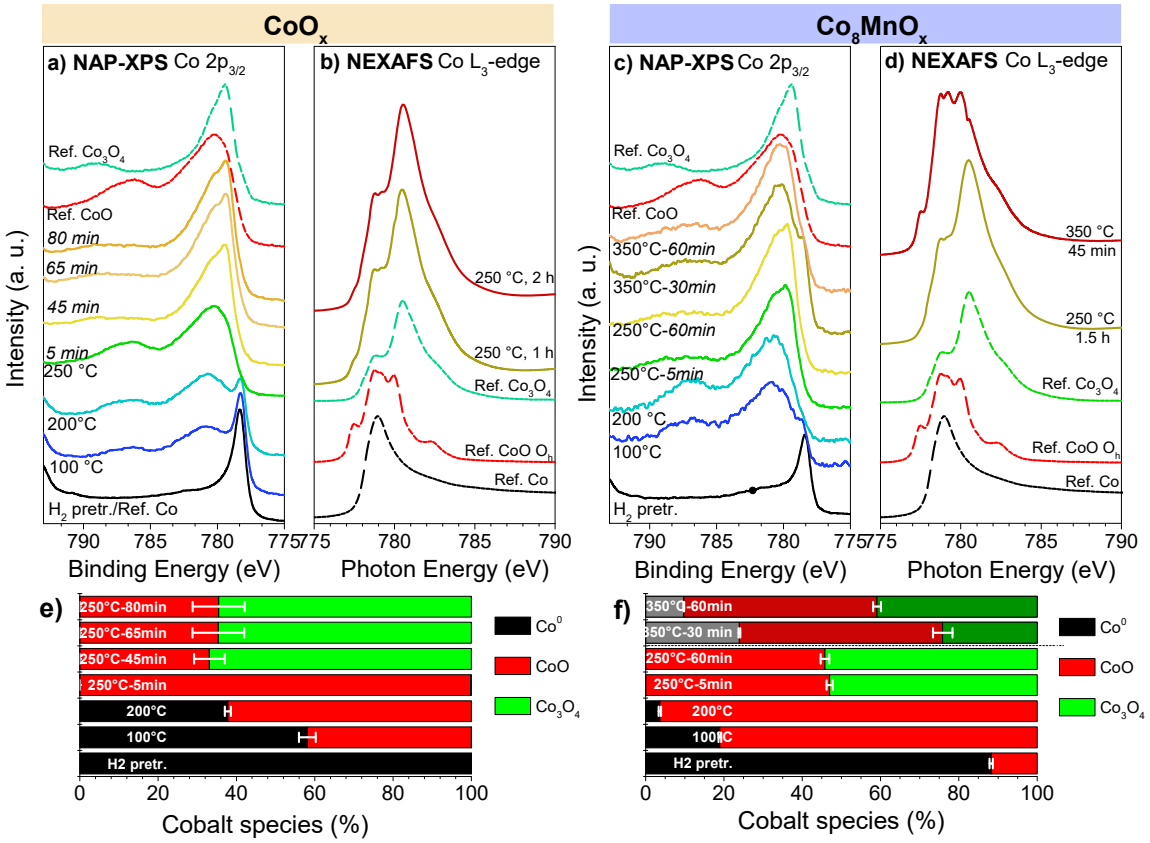

Figure 3. In situ NAP-XPS and NEXAFS spectra of a,c) Co $2p_{3/2}$ (hν = 1020 eV) and b,d) Co L_3-edge recorded on pure CoO_x (a,b) and Co_8MnO_x (c,d) after H_2 pretreatment and during COPrOx at various temperatures. Operating conditions: 0.5 mbar of 1% CO, 1% O_2, 50% H_2 and He, from room temperature to 250 °C (or 350 °C in case of Co_8MnO_x). The bar graphs e) and f) show the percentage of each cobalt oxidation state calculated by deconvolution of the relevant Co 2p peaks.

3.3.2 Analysis of the Mn oxidation state and distribution

The manganese oxidation state is discussed next. The NAP-XPS Mn $2p_{3/2}$ and NEXAFS Mn L_3-edge spectra of Co_8MnO_x are shown in figures 4a and b respectively. The distribution of Mn oxidation state (figure 4c) was estimated by deconvolution of the Mn 2p peaks. In accordance with several works devoted to Mn curve fitting [79–81], the peaks of Mn^{2+} (MnO) and Mn^{3+} (Mn_2O_3) appear at very similar binding energies (BEs) (around 641 eV), but can be differentiated by the characteristic shake-up satellite at 647.5 eV only visible in the MnO peak. The Mn^{4+} state (MnO_2) has similar peak profile with Mn^{3+} but is shifted by 1 eV to higher BEs. The different

oxides can be distinguished better by their Mn L_3-edge NEXAFS spectra which show distinctly different features [61].

During H_2 pretreatment manganese is reduced to the lowest oxidation state observed in this work, which is Mn^{2+}. This is quite evident also by the satellite feature at the Mn 2p photoelectron peak and the similarity of the Mn L_3-edge NEXAFS spectra with MnO reference (green dotted line). Mn^{2+} was progressively oxidized to Mn^{3+} and M^{4+} during the heating step to 250 °C under the COPrOx feed. However, at 350 °C part of Mn^{4+} reduces back to Mn^{3+}/Mn^{2+} states as also confirmed by the Mn L_3-edge, matching reasonably well the Mn_3O_4 spinel oxide (or $MnO{\cdot}Mn_2O_3$). This redox behavior is similar to the one observed for cobalt, *i.e.* oxidation up to 250 °C and partial reduction at higher temperature, showing that temperature and gas phase composition define the redox ability of the gas phase.

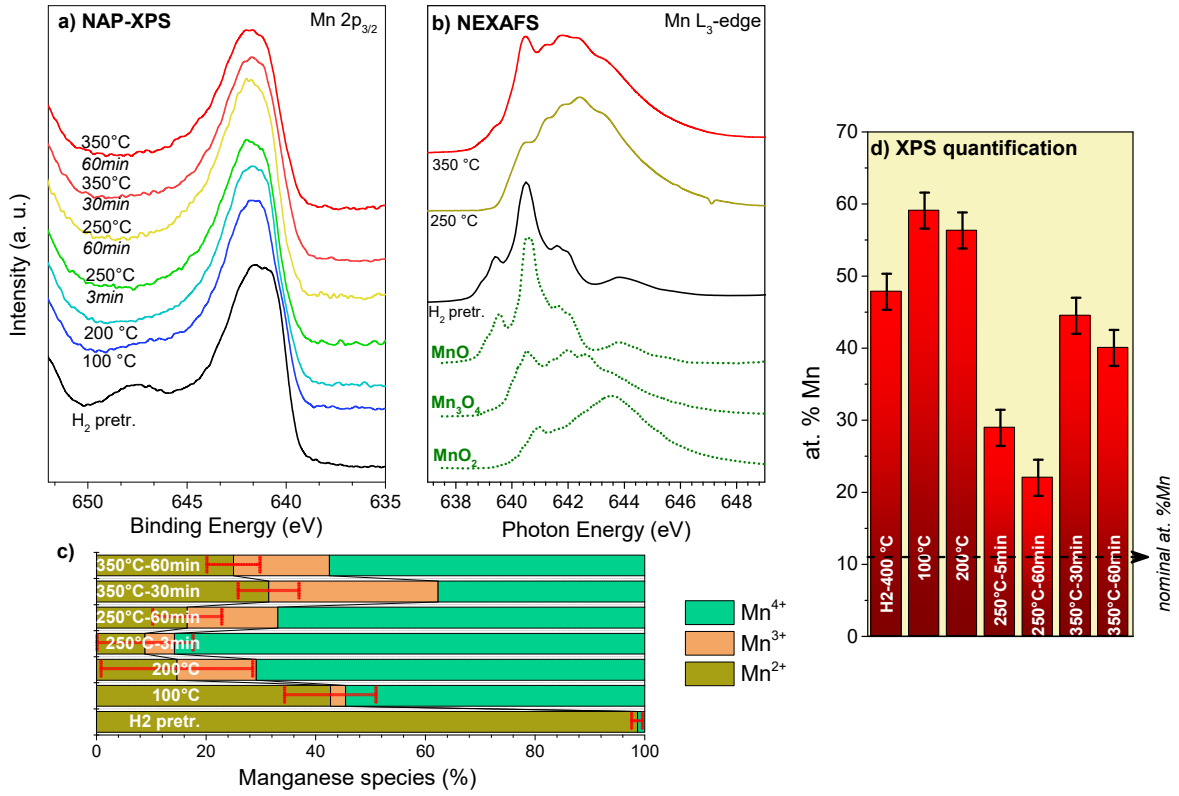

Figure 4. In situ NAP-XPS and NEXAFS spectra of a) Mn $2p_{3/2}$ (hν = 880 eV) and b) Mn L_3-edge recorded on Co_8MnO_x at room temperature, after H_2 pretreatment and during COPrOx at various temperatures. Reference Mn L_3-edge spectra were retrieved from reference [61]. Operating conditions: 0.5 mbar of 1% CO, 1% O_2, 50% H_2 balance He, from room temperature to 250 °C and 350 °C. c) Bar graph showing the percentage of each Mn oxidation state calculated by deconvolution of the Mn 2p peaks shown in (a). d) The evolution of Mn concentration (metal at. %) under various reaction conditions calculated from the Mn 2p and Co 2p NAP-XPS spectra. The estimated analysis depth to be 2.2±0.1 nm.

The Mn/(Mn+Co) atomic ratio (hereafter at. %Mn) shown in figure 4d was calculated based on Mn 2p and Co 2p spectra. Four excitation photon energies, corresponding to two analysis depths (or information depths) were used (see Table S2). It is clear that for all examined temperatures the surface concentration of Mn is much higher than the 12% nominal value. A significant drop

of %Mn is observed at 250 °C in the COPrOx, while at 350 °C the %Mn rises back again. Comparison of the two analysis depths (Table S2) reveals that the %Mn is systematically higher at the most surface sensitive mode (around 2.2 nm), which means that Mn is mainly segregated over cobalt. This suggests no extensive mixed oxide phase formation, in agreement with the XRD results discussed above. One should note that the at. %Mn found from NAP-XPS is much higher than the one given from STEM-EDX (figure 1). This should be expected for Mn-surface enriched samples based in the differences in the analysis depth of the two methods (about 4 nm for XPS and 2000 nm for EDX).

3.4 Redox stability of Co_8MnO_x measured by *in situ*–NEXAFS at 1 bar

The NAP-XPS and NEXAFS results identified the oxidation states of cobalt and manganese that are involved in the COPrOx reaction providing some useful insights in the reactivity in the fixed-bed reactor experiments. However, the relatively low operating pressure (0.5 mbar) of NAP-XPS raises some doubts about the extrapolation of the redox behavior of the catalyst under atmospheric pressure, which is essential to correlate NAP-XPS and fixed-bed reactor. To clarify this point we performed *in situ* NEXAFS experiments at 1 bar on Co_8MnO_x under reducing (100% H_2) and oxidizing (10% O_2/He) atmospheres [59]. Figure 5 shows the Co L_3-edges (a,b) and Mn L_3-edges (c,d) of calcined Co_8MnO_x upon reducing in H_2 and subsequently re-oxidized in 10% O_2/He. The relative concentration of each oxidation state, estimated by linear combination fit analysis (see figure S9), is included in the right part of each graph. Initially the Co L_3-edge corresponds to the Co_3O_4 oxide (figure 5a) while reduction to about 50% of CoO is observed at 250 °C. The Mn L_3-edge after calcination (figure 5c) resembles the one of MnO_2, but in H_2 this phase reduces gradually to Mn_3O_4 (at 200 °C) and MnO (at 250 °C).

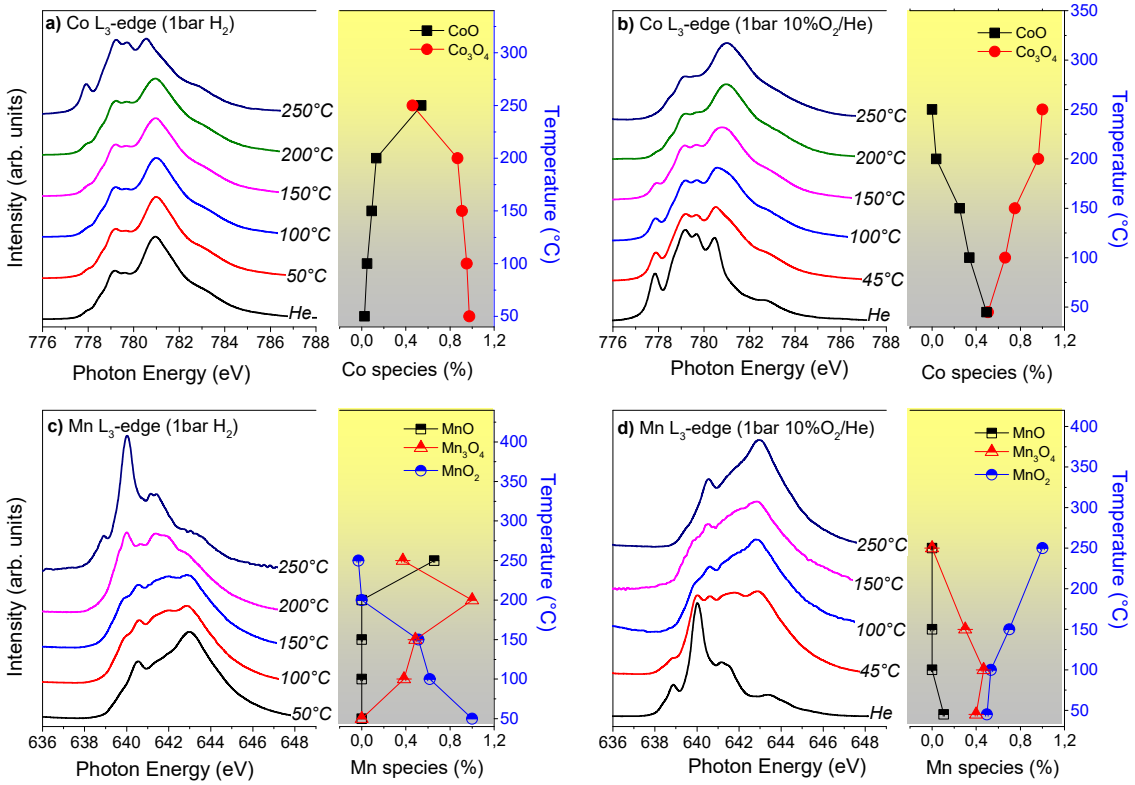

Figure 5. *In situ* Co L_3-edge NEXAFS spectra of Co_8MnO_x catalysts recorded at a) 1 bar H_2 and b) 1 bar 10%O_2 in He between 50-250°C. The corresponding Mn L_3-edge is shown in c) and d), respectively. The evolution of the different Co and Mn oxidation states/phases estimated by linear combination fit analysis using reference spectral profiles of relevant Co- and Mn-oxides are included in the right part of each graph.

Exposure of the pre-reduced Co_8MnO_x to 10% O_2 (figures 5b and d) initiates a gradual oxidation of MnO to MnO_2 and CoO to Co_3O_4. Notably, oxidation of MnO is facile since the catalyst is transformed to a mixture of Mn_2O_3/MnO_2 already at 50 °C, while at 150 °C more than 70 % of manganese has been oxidized to MnO_2. In 10% O_2, both cobalt and manganese are more oxidized as compared to the COPrOx mixture investigated with NAP-XPS. This is expected from the more oxidizing gas feed of 10% O_2. Nevertheless, the aforementioned NEXAFS results suggest that the mixed oxidation states found at the surface of Co_8MnO_x catalyst in the 0.5 mbar NAP-XPS experiment can be maintained even at atmospheric pressure.

3.5 Operando *AlKα source* NAP-XPS measurements

In this paragraph cobalt catalysts (Co, Co_8MnO_x and $CoMn_8O_x$) with identical oxidation states are compared with or without Mn addition, in order to distinguish the Mn effect on the COPrOx selectivity. As described in the experimental part the reaction conditions (reactor volume, reactants feed and flow) are different from those of the synchrotron-based experiments having notable effect on cobalt oxidation state [63]. After the H_2 pretreatment at 400 °C, the surface of pure CoO_x was fully reduced to Co^0 while that of the Mn-based catalysts remained as CoO. This

difference is consistent with the findings of H_2-TPR measurements (figure S4) which showed that Mn addition shifts CoO_x reduction to higher temperature. However, in this case CoO is more resistant to reduction as compared to the synchrotron-based NAP-XPS reactor (figures 3c and 3f).

Figure 6 displays the Co $2p_{3/2}$ peaks of the three catalysts recorded in COPrOx at three characteristic temperatures. For pure CoO_x, the intense peak at 778.4 eV due to Co^0 [82] shifts to 780.6 eV, indicating a progressive oxidation of Co^0 to CoO [83] (figure 6d). On the contrary, in the case of Co_8MnO_x and $CoMn_8O_x$ catalysts, cobalt remains as CoO at all reaction temperatures. The analysis of the Mn $2p_{3/2}$ peaks (figure S10), shows that Mn is progressively oxidized but remains always in a mixed $MnO/Mn_2O_3/MnO_2$ state. A comparison between the two Co-Mn samples suggest that Co_8MnO_x promotes Mn^{2+} and Mn^{4+} while $CoMn_8O_x$ favors more Mn^{3+} species.

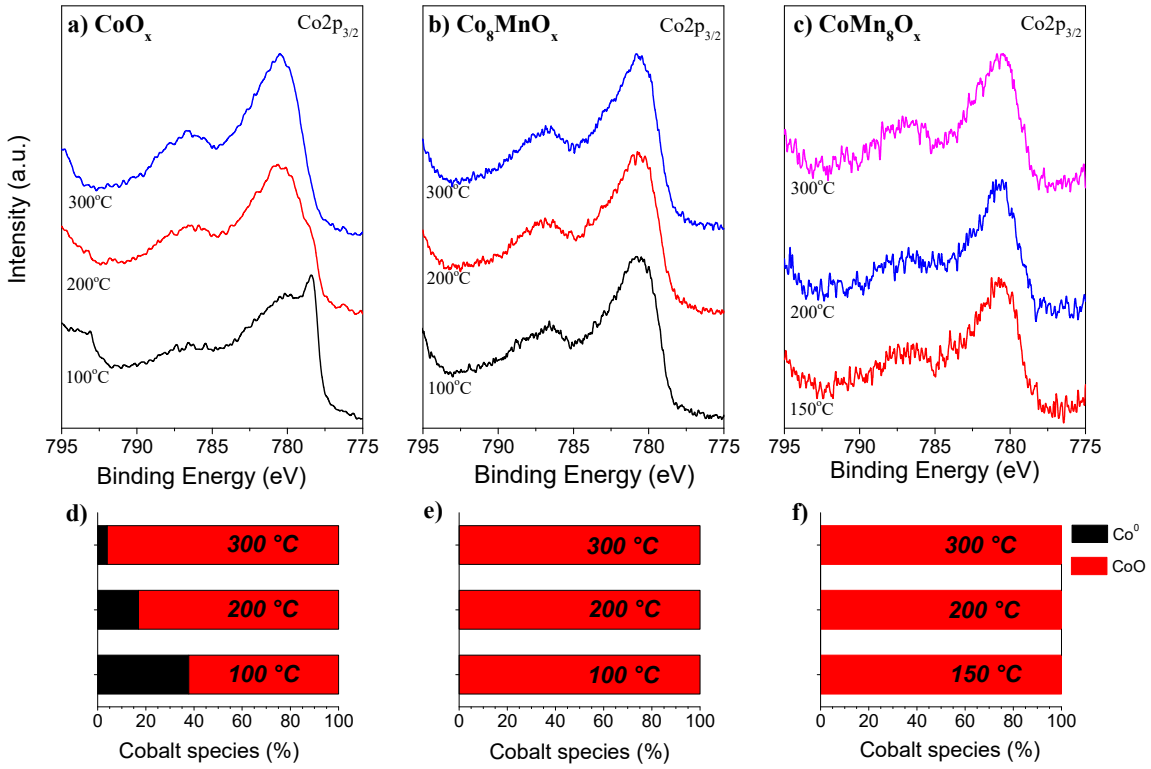

Figure 6. *In situ* NAP-XPS spectra of Co $2p_{3/2}$ on a) pure CoOx, b) Co_8MnO_x and c) $CoMn_8O_x$ recorded during COPrOx at various temperatures. The distribution of cobalt species resulting from Co $2p_{3/2}$ peak analysis is shown in the bar plots: (d,e and f) below of each set of spectra. Operating conditions: 1 mbar of 1% CO, 1% O_2 and 98% H_2, from room temperature to 300 °C.

The X_{CO} and X_{O2}, as well as the CO_2 and CH_4 selectivities (S_{CO2} and *rel.*S_{CH4} respectively) were calculated from the QMS signal and are shown in figure 7. In all cases the CO and O_2 conversion (figures 7a and 7b) appear at around 100 °C and increases at higher temperature. The X_{CO} is very similar for Co_8MnO_x and CoO_x catalysts up to 250°C, while for $CoMn_8O_x$ it is significantly lower (figure 7a). A similar trend is also observed in the S_{CO2} (figure 7c), with $CoMn_8O_x$ having the

lowest S_{CO2} of the three catalysts, while those of Co_8MnO_x and CoO_x are comparable. The relative selectivity of CO to CH_4 (figure 7d), is practically zero for Co_8MnO_x and $CoMn_8O_x$, but for CoO_x increases rapidly above 200 °C reaching its maximum value at 300 °C. This implies a boost of hydrogenation reactions (reaction 3 and 4) on this catalyst and explains the high X_{CO} of CoO_x at 300 °C (figure 7a). Clearly for this sample CO is consumed via the methanation reaction (reaction 3) at 300 °C while the Co_8MnO_x catalyst becomes more selective to H_2O as expected in this temperature region.

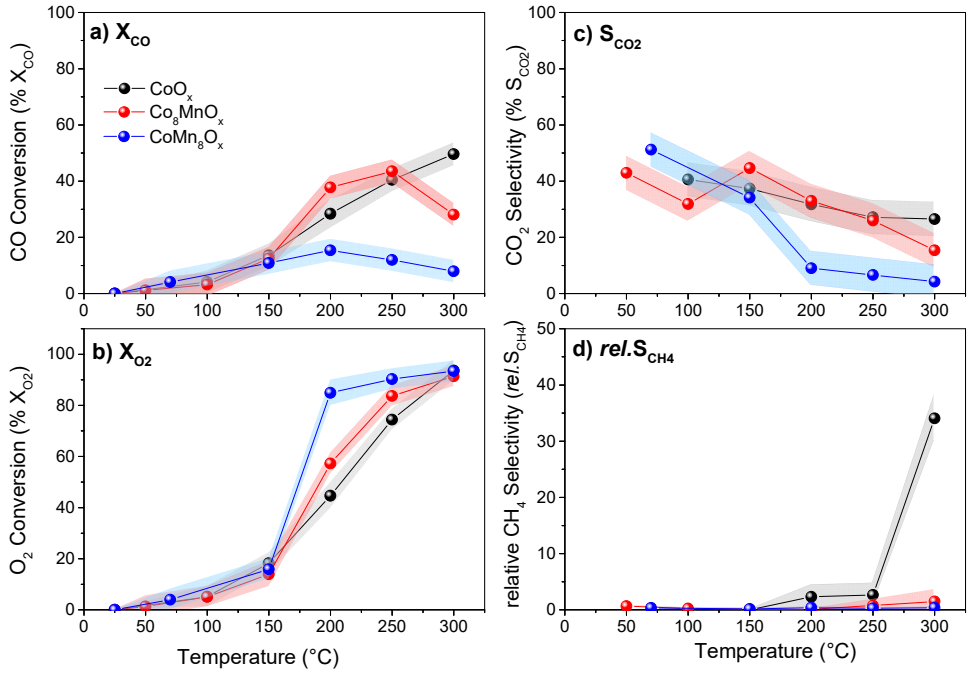

Figure 7. Conversion of *(a)* CO (X_{CO}) and *(b)* O_2 (X_{O2}). The *(c)* selectivity of O_2 to CO_2 (S_{CO2}) and *(d)* the relative selectivity of CO to CH_4 (*rel.*S_{CH4}) calculated from *on line* mass spectrometry data recorded on pure CoO_x (●) Co_8MnO_x (●) and $CoMn_8O_x$ (●) during NAP-XPS measurements under COPrOx conditions. Prior to the activity tests, the samples were pretreated in the XPS chamber under 1 mbar of H_2 at 400 °C for 1 h.

3.6 Effect of Mn-Co nanoscale spatial distribution on Co oxidation state during COPrOx

NAP-XPS data in paragraph 3.3 suggest that despite the enchantment of CoO stability by Mn, a significant amount of Co_3O_4 is formed over Co-Mn catalysts under reaction conditions. In this paragraph the effect of Mn on CoO stabilization of is investigated in detail, taking into account the significant diversity at the Co_8MnO_x morphology revealed by SEM-EDX and STEM-EDX. The discussion focuses on the Co_8MnO_x catalyst since it has the best catalytic performance.

The apparent surface area analyzed by the employed synchrotron-based NAP-XPS setup is largely defined by the spot size of the incident X-ray beam, as the electron collecting cone of the analyzer is larger than 1 mm. Under the current working conditions, the X-ray spot on the sample is a parallelogram with dimensions of 180×10 μm^2. The small area spot analysis of synchrotron-based NAP-XPS can be used to provide details regarding the effect of Mn on the oxidation state of cobalt. To do so, NAP-XPS spectra were collected in two different spots of the

catalyst pellet, by shifting the sample lateral position with respect to the analyzer, while keeping the sample under the same reaction conditions (250 °C in COPrOx). In this way we could directly detect the oxidation state of cobalt in areas that are rich or poor in Mn and draw conclusions about the possible Mn effect over the redox stability of cobalt oxides.

The Co 2p spectra recorded at two characteristic sample positions are shown in figure 8. The first (*spot 1*) has a high Mn concentration, and the second (*spot 2*) has a low Mn concentration. For comparison the results presented in figure 3 are collected in the position of spot 1. Based on Co 2p peak deconvolution it becomes evident that CoO concentration is higher in areas that contain more Mn *(spot 1)*, while Co_3O_4 prevails in areas dominated by cobalt *(spot 2)*. In particular, the CoO/Co_3O_4 from 44/56 in Mn-rich area of the catalyst drops to 30/70 in the Co-rich area. Please note that this ratio is close to the one observed for the parent pure CoO_x. The CoO/Co_3O_4 ratio in the two spots is practically the same for the two analysis depths (not shown), which means that there is no depth distribution between CoO and Co_3O_4 and within the outer 4 nm the two cobalt oxides are homogeneously mixed.

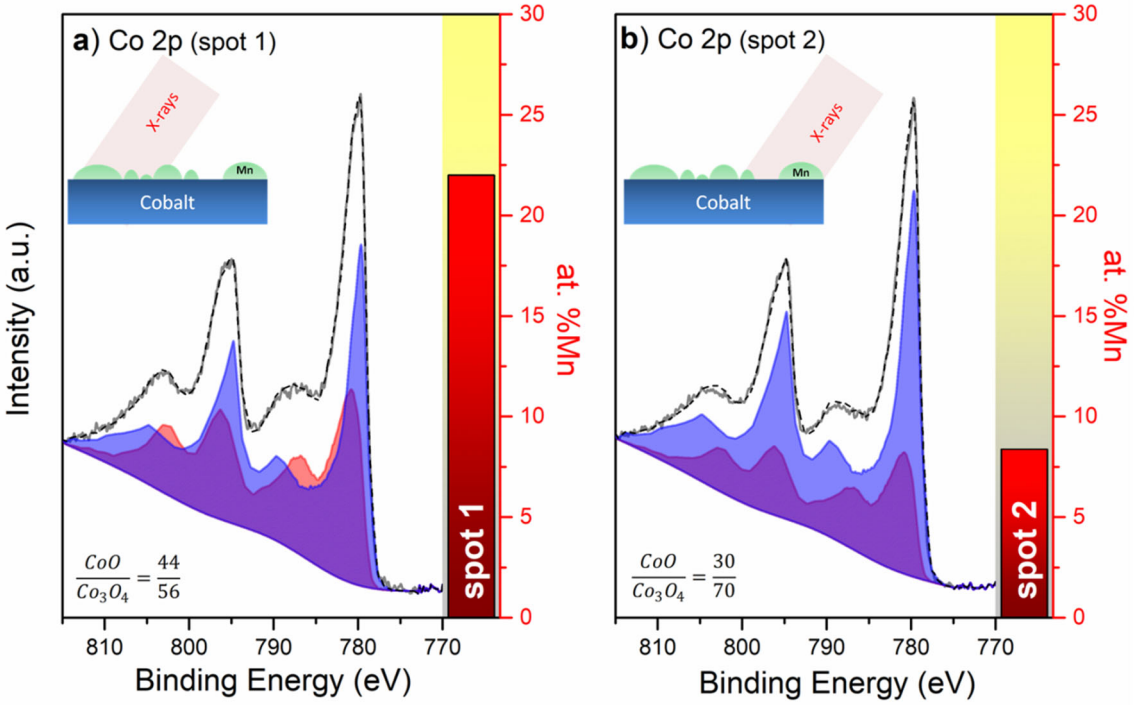

Figure 8. The Co 2p spectra recorded at 250 °C over two different areas (spots) of Co_8MnO_x catalyst under identical COPrOx reaction conditions. Each Co 2p peak was deconvoluted into CoO (dark purple peak) and Co (light purple peak) components. The bar in the right part of each figure shows the at. % Mn calculated by the Mn 2p and Co 2p peaks recorded at each spot. A schematic representation of the expected morphology in each spot based on the % Mn is included at the top-left of each figure.

The effect of Mn on Co oxidation state in areas where the two elements are in close proximity is addressed by high resolution STEM (HRSTEM). The inhomogeneity of Co_8MnO_x catalyst can be

used as an opportunity to examine, at the same aggregate, uncovered and Mn-overlapping Co areas at the nanoscale. The STEM-EDX images can serve as a guide to identify the two areas on an aggregate. Figure 9 presents HRSTEM images of spent Co_8MnO_x catalyst, collected in areas exclusively occupied by Co, as manifested by the STEM-EDX image shown in the left-up panel. Similar images of other Co_8MnO_x aggregates can be found in figure S11. The interplanar spacing (lattice fringes) of 0.24 nm measured in area 1 (marked by white lines) corresponds to Co_3O_4 (311) lattice planes. The presence of Co_3O_4 is confirmed by the fast Fourier transform (FFT) diffraction pattern of a selected area (area 3), which clearly shows the characteristic diffraction spots due to the different Co_3O_4 lattice planes.

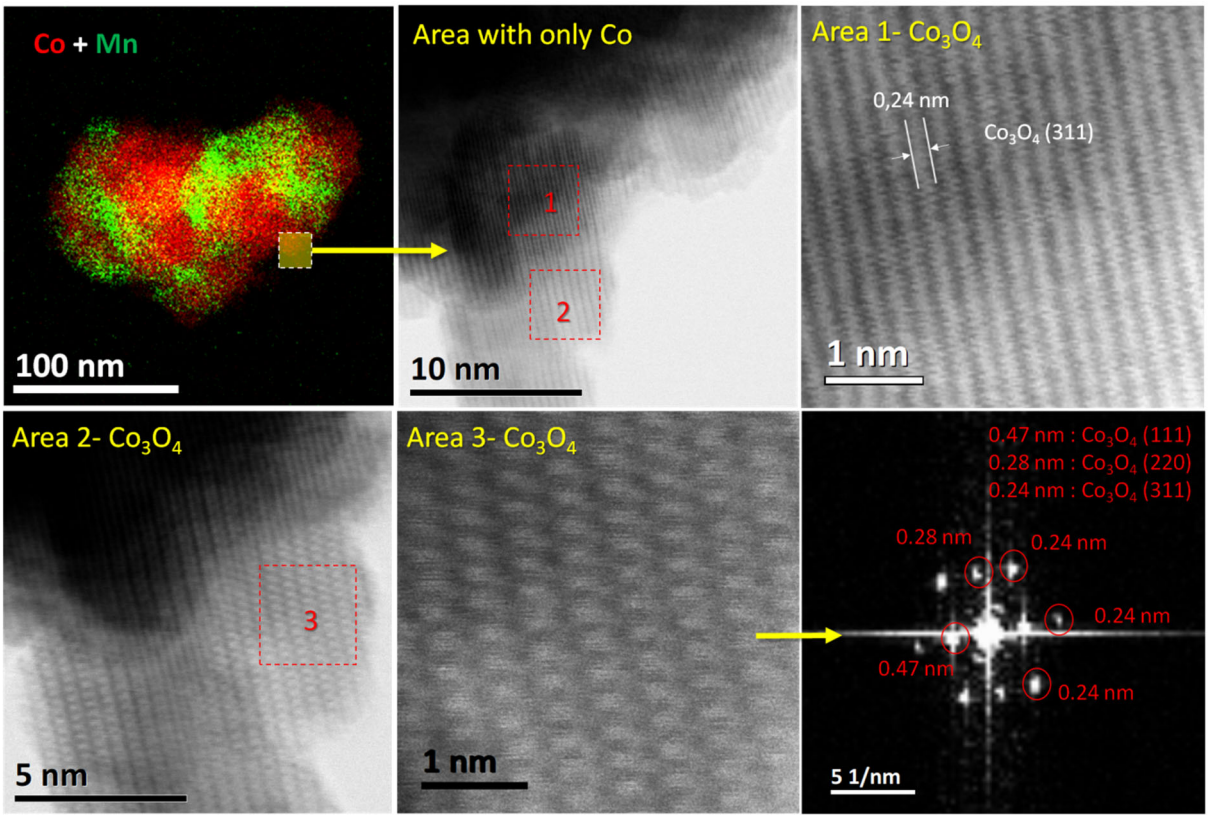

Figure 9. STEM-EDX (top left) image of the spent Co_8MnO_x catalyst and the high resolution bright field STEM images derived from catalyst areas composed *exclusively by cobalt*. The interplanar spacing is indicated by two parallel lines. The squares indicate the part of the low magnification image from which the high-resolution images are derived. The FFT diffraction pattern at the bottom-right corresponds to spot 3 beside.

Similar analysis was also carried out in aggregate areas where both Co and Mn signals were indicated by STEM-EDX. Figure 10 shows characteristic HRSTEM images and FFT patterns recorded in such an area, while additional images can be found in figures S12. The HRSTEM at the Co and Mn interface area evoke a border between the two oxide phases indicated in the image by a red-dashed line. The measurements of the lattice fringes, at the two sides of this border, are consistent with MnO_2 and CoO, respectively. The presence of CoO in the vicinity with manganese oxide is evidenced also in the FFT patterns taken in the same area. Analysis of other

aggregates presented in figure S12, suggest that stabilization of CoO phase in areas close to Mn is a general feature of the Co_8MnO_x sample in complete accordance with NAP-XPS results of figure 8.

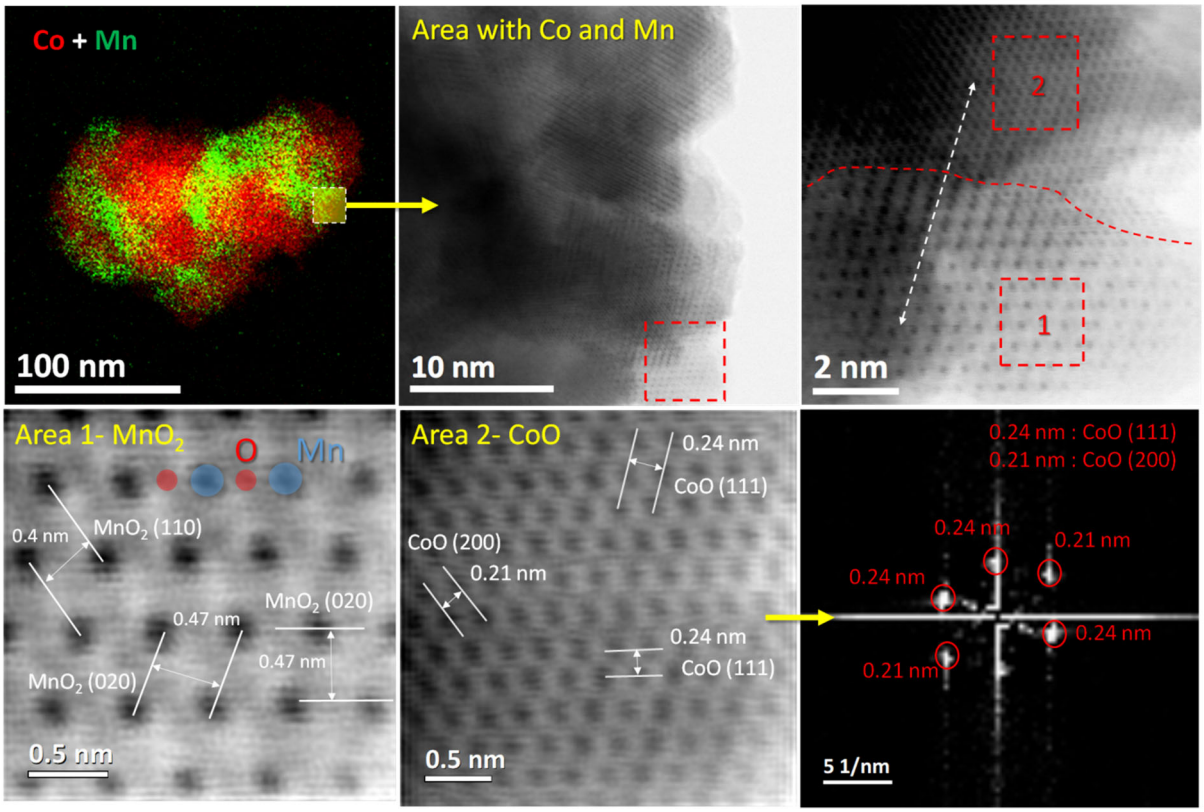

Figure 10. STEM-EDX (top left) image of the spent Co_8MnO_x catalyst and the high resolution bright field STEM images derived from catalyst areas where *Co and Mn overlap*. The interplanar spacing is indicated by two parallel lines. The squares indicate the part of the low magnification image from which the high-resolution images are derived. The Mn and O atoms of MnO or MnO_2 are displayed in blue and red respectively and are superpositioned on the image. The FFT diffraction pattern at the bottom-right corresponds to image beside.

The correlation between Mn excess and higher CoO concentration implies that Mn helps to stabilize the CoO phase under conditions for which pure cobalt tends to oxidize to Co_3O_4 (e.g. figure 3a and 3b). Based on our previous results [48] CoO is more active than Co_3O_4 for COPrOx. Therefore, partial stabilization of CoO in the Co_8MnO_x catalyst is expected to enhance the activity of this catalyst as compared to pure cobalt. In addition, Mn also helps to stabilize the morphology of the oxide, as BET analysis shows identical surface areas before and after PrOx (not shown). However, STEM-EDX and SEM-EDX images manifest that there are areas on the Co_8MnO_x surface where cobalt is not in contact with Mn. These areas are expected to preserve the redox properties of the parent material (i.e. CoO_x), therefore being prone to oxidation to Co_3O_4 and to reduction towards Co^0 depending of the COPrOx reaction temperature.

We now discuss the possible CoO stabilization mechanism in areas close to manganese. HRSTEM images clearly show that the lattice fringes close to the Co-Mn interface correspond well to those of the individual metal oxides. There is no evidence about mixed phase formation at

their interface, for example a mixed Co-Mn oxide. On a macroscopic scale, formation of mixed Co-Mn oxide may be detected in XRD or by the shift of the Co 2p satellite peak [84]. As discussed in paragraph 3.1 there are no diffraction lines in XRD indicating mixed phases. Comparison of the Co $2p_{3/2}$ spectra between Co_8MnO_x and CoO_x samples in cases where Co^{2+} is the dominant oxidation state (see figure S13) do not reveal any evident difference in the shake-up satellite peak position (around 786.8 eV). Besides, the Co L-edge NEXAFS spectra of the two samples are also similar (see figures 3b and 3d). Therefore, the similarities of both XPS and NEXAFS spectra between the two catalysts, together with the HRSTEM and XRD analysis results discussed above, suggest that Mn and Co do not form a mixed Co-Mn oxide phase but rather keep separated as individual oxides in close proximity (similar to a composite). Therefore stabilization of CoO should be attributed to geometric effects and to phenomena taking place at the Co-Mn interface, as for example facile exchange of O^{2-} ions, which cannot be detected here. An analogous synergetic interaction at the interface between CuO and MnO_x over CuO/cryptomelane catalysts, has been reported to promote the lattice oxygen mobility and to increase the CO-PrOx catalytic activity [17].

4 Discussion

The catalytic tests at 1 bar showed that the addition of Mn on Co (Co_8MnO_x) promotes the COPrOx activity. On the downside, above 250 °C, the CH_4 selectivity increases. At this point we will try to elucidate the role of the manganese promotion on cobalt reactivity by synthesizing the results presented above. Before doing so, we highlight the two different paths in which Mn may influence the reactivity. The first is related to the increase of the catalytic surface area and the partial stabilization of the CoO phase, known to have positive effect on the catalytic activity and O_2 selectivity to CO_2 [48]. We consider this path as an *indirect effect* of Mn on the reactivity in a sense that Mn stabilizes CoO, but the reaction mainly involves cobalt sites. The second path considers that Mn influences the reactivity by directly participating in the reaction, independently of its effect on the cobalt oxidation state. To distinguish the two pathways we will call this the *direct effect* of Mn on the reactivity. For conciseness, the discussion focuses mainly on the comparison between CoO_x and Co_8MnO_x since these catalysts are based on the same CoO nanopowder.

4.1 The effect of manganese on the COPrOx activity

BET surface area measurements after reduction indicate that addition of Mn on cobalt enhances the exposed surface giving almost 4.5 times higher specific surface area for Co_8MnO_x than that of pure CoO_x. In general, higher surface areas should lead to better reactivity, provided that the increase of the exposed surface atoms is proportional to the increase in the number of active catalytic sites. The surface analysis results presented above makes it clear that the cobalt

atoms reside in a variety of states and environments (e.g. oxidation states, contact or not with Mn atoms *etc.*). There are also previous evidences [48] that each cobalt state exhibits different catalytic activity in the given reaction, which renders the quantification of the surface active sites problematic on our powder catalysts. Nevertheless, the best possible approximation to compare the reactivity of pure and Mn-promoted Co catalysts remains to normalize the conversion to the total number of the exposed Co atoms (i.e. surface area). However, although for pure CoO_x the BET surface area gives a measure of the number of exposed Co atoms, in case of Co_8MnO_x this in not true since both Mn and Co sites are counted. Besides, as shown by STEM-EDX and NAP-XPS, the majority of Mn is segregated over Co reducing the accessibility of the latter to the reactants.

Unfortunately, it is not possible to measure directly the uncovered surface area of cobalt on Co_8MnO_x catalyst, but quantitative simulation of the XPS peak intensities can help to get an approximate estimation of this number. In order to minimise the effect of the inhomogeneity in the surface distribution of Mn over Co (see figure 8) the Co_8MnO_x was measured after reducing, oxidizing and UHV annealing treatments using a dual anode X-ray source with analysis area of 12×12 mm^2. The 3 measurements gave an average $R_{Mn}=\frac{Mn\ 2p}{Mn\ 2p+Co\ 2p}$ ratio of 0.19±0.1. The quantitative simulations of Mn 2p and Co 2p peaks using SESSA vs 2.1.1 software (see supporting information 13) concluded that for Co_8MnO_x the experimental R_{Mn} corresponds to about 24% of exposed/uncovered cobalt area as compared to the overall surface of the catalyst. Although this number seems low, if compared to the bulk composition of Co_8MnO_x (~89%), it is justified by the preference of Mn to segregate over Co suggested by the characterization. Consequently, and according to the BET measurements shown in table 1, the specific surface area of exposed cobalt atoms over Co_8MnO_x catalysts is around 1.6 m^2g^{-1} (the rest 4.9 m^2g^{-1} of the surface is supposedly covered by Mn). Although as mentioned above this is a rough estimation, it suggests that the differences in the X_{CO} of the two catalysts (figure 2a) might not be explained just on the grounds of their surface area differences.

Thus, the stability of CoO phase on Mn-promoted cobalt catalyst shown in figure 3, may be an additional reason of the high Co_8MnO_x activity. This can be exploited further by comparing the qualitative differences between Co_8MnO_x and CoO_x in the catalytic tests of figure 2 (1 bar) and figure 7 (1 mbar or $1x10^{-3}$ bar). In particular, at 1 mbar (low flow experiment) the X_{CO} is similar for the two catalysts (figure 7a), but it is very different at 1 bar (high flow experiment, figure 2a). The similarity of X_{CO} at 1 mbar experiment suggests that in this case the difference in their surface area do not have a pronounced effect on the reactivity,. AlKα source NAP-XPS shows that at 1 mbar CoO dominates both CoO_x and Co_8MnO_x catalysts and as expected [48], similar cobalt surface states give comparable X_{CO} in figure 7. In contrast, at 1 bar, Co_3O_4 formation is favored over CoO_x catalyst as anticipated by synchrotron NAP-XPS (figure 3). Co_3O_4 has a negative effect on the X_{CO} [48], rationalizing the lower activity of CoO_x catalyst in figure 2a as compared to

$CoMn_8O_x$ (schematically shown in figure 11).

The above arguments point to the fact that Mn-promotion effect on X_{CO} is related to surface area increase and stabilization of the CoO state. Both effects can be considered as *indirect effects*, and no indication was found pointing that manganese promotes CO oxidation during COPrOx. Therefore, the previously reported high MnO_x activity for CO oxidation [50] seems not to be preserved in H_2 presence.

4.2 The effect of manganese on the COPrOx selectivity

We turn now our attention on the effect of Mn on the COPrOx product selectivity. We recall here that the desired product of COPrOx reaction is CO_2, but there are two other common by-products of the reaction, namely H_2O and CH_4, which should be avoided since their formation consumes valuable H_2. Therefore, a selective COPrOx catalyst should boost the production of CO_2 (reaction 1) and minimize these of H_2O (reaction 2) and CH_4 (reactions 3 and 4). In principle, S_{CO2} differentiates reaction 1 from 2, while S_{CH4} reaction 1 from 3 and 4. However, at conditions where CO is hydrogenated to produce CH_4, the S_{CO2} will increase independently of the reactions 1 and 2. Therefore to avoid ambiguities, the S_{CO2} between different samples will be compared up to 200 °C, hence before CH_4 production.

We start with the discussion of S_{CO2}, while continuing to use arguments based on catalytic tests in figures 2 (1 bar) and 7 ($1x10^{-3}$ bar). In both experiments the S_{CO2} of CoO_x and Co_8MnO_x are very similar up to 200 °C. This observation suggests that the addition of small Mn quantities on cobalt does not have direct effects on the S_{CO2}. However, in Mn excess (i.e. $CoMn_8O_x$ catalyst), both 1 mbar and 1 bar catalytic tests implies that the undesired H_2 oxidation reaction (reaction 2) is promoted leading to the formation of water. This is supported by the *operando* NAP-XPS measurements, which show distinct differences in the S_{CO2} between Co_8MnO_x and $CoMn_8O_x$, while in both catalysts the surface is dominated by CoO (figure 6). Therefore, it appears that in COPrOx, manganese oxides favour H_2 oxidation over CO oxidation (see figure 11).

Another difference between the results of figures 2 and 7 is noticed in the selectivity of CO to CH_4 (S_{CH4}). In particular, at 1 bar the Co_8MnO_x has higher S_{CH4} than CoO_x while at 1 mbar the reaction trend among the two catalysts is reversed. CH_4 is produced by the methanation/hydrogenation of CO and/or CO_2 according to reactions 3 and 4. Methanation reactions are known to increase with temperature and with the presence of reduced cobalt (Co or CoO) [13]. This can explain why in 1 bar test, S_{CH4} of Co_8MnO_x is higher since according to figures 3 and 5 this catalyst is expected to have higher proportion of reduced cobalt. However, at the low flow experiment (1 mbar), where both catalysts are dominated by CoO, only pure CoO_x catalyst shows the expected high S_{CH4}, while for Co_8MnO_x the S_{CH4} is about 20 times lower. This result indicates that Mn helps to suppress CO methanation reactions (figure 11) at high temperature and most probably moderates the S_{CH4} at 1 bar, which without its addition could be

even higher. This argument is in line with the absence of CH_4 production in case of $CoMn_8O_x$ catalyst (figure 7d). Note that reduced cobalt is beneficial for PrOx at moderate reaction temperatures, but might lead to worse S_{CH4} at higher temperature where CH_4 formation is thermodynamically favored. Although the mechanism via which Mn influences the CH_4 selectivity cannot be directly deduced from our studies, evidently is not related to the stabilization of CoO state and therefore is considered as a *direct effect* of Mn on the cobalt reactivity.

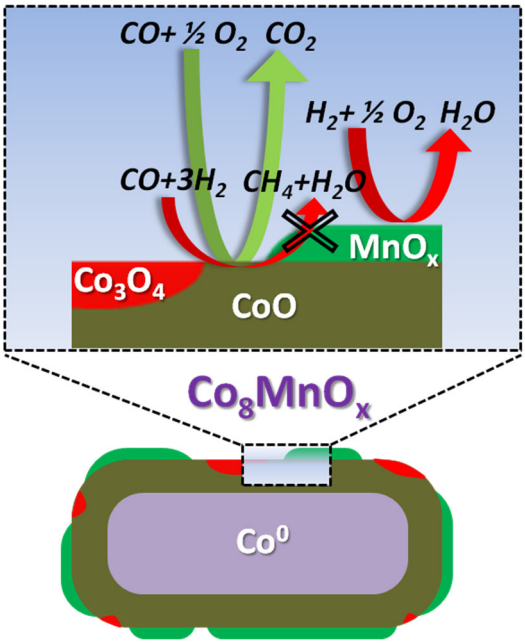

Figure 11. Schematic representation of the arrangement between cobalt and manganese oxides on the surface of Co_8MnO_x catalysts and the proposed COPrOx reactivity paths promoted at each location of the catalyst.

Overall, we have shown that Mn-promotion increases the structural stability of cobalt and, in this way, enhances the COPrOx activity. However, the interaction of Co and Mn is rather weak and their segregation is facilitated either during pre-treatment or under reaction conditions, leaving large areas of the catalyst where Mn and Co are not in contact. In these areas Co_3O_4 is readily formed under reaction conditions with negative effects on the CO conversion and S_{CO2} selectivity. Most probably, more complex synthesis methods, than the impregnation or co-precipitation used in this work, could be elaborated to enhance the distribution of Mn on Co and stabilize the CoO phase, targeting to a more active and selective Co-Mn catalyst. However, the significant evolution of the Mn surface concentration under reaction conditions (figure 4d), suggests that in long term stability might be an issue for Co-Mn catalysts. In addition to that, a commercially viable cobalt-based COPrOx catalyst should employ relatively simple synthesis methods, like those used in this work, which can scale-up easily. Therefore, the effort to enhance the stability of CoO in cobalt-based COPrOx catalysts should be pursued, possibly by testing other promoters with higher synergy with cobalt. As we have recently shown vanadium might be a very promising choice in this direction [85].

5 Conclusions

In this work Mn-Co catalysts were synthesized and their performance in the COPrOx reaction was evaluated. The addition of Mn on Co (Co_8MnO_x) enhances the structural stability of the catalyst and led to a significant increase in the catalyst performance. We show how the local structure of the catalytic particles may influence the redox stability of cobalt affecting the COPrOx performance. *Operando* spectroscopy and atomic-resolution microscopy indicate that the CoO phase is partially stabilized in the presence of Mn, which is expected to contribute to the higher catalytic activity. Depending on the operating conditions (time, temperature, gas mixture, etc.), MnO can be progressively oxidized into MnO_2 and reduced back to MnO. Excess of MnO_x on the catalyst's surface was correlated with high O_2 consumption through the unwanted H_2 oxidation. Although Mn addition helps to stabilize the CoO phase promoting the catalytic activity, the synergy of the two oxide phases is limited by phase segregation. The dynamic transformation of the surface oxidation state and composition during COPrOx reaction was directly evident in the spectroscopic studies under working conditions. Thus, to the authors' opinion further efforts are needed in order to fabricate promoted cobalt-based catalysts able to stabilize the CoO phase on their surface for sufficiently long reaction periods.

Acknowledgments

LZ and DKC would like to thank the China Scholarship Council (CSC) for supporting their studies at ICPEES. MB acknowledges financial support from Strasbourg University via the IdEX-2018 (Post-doctorants) project. EB and DHL acknowledge the support from PRIN-2017 MOSCATo, project n. 2017KKP5ZR. We thank Prof. C. Petit for the useful and constructive discussions, Dr. T. Dintzer for the SEM-EDX and Prof. A. Boos for the ICP measurements. L. Braglia, A. Martini, D. Salusso and M. Signorile are acknowledged for their help during the in situ NEXAFS data collection on APE-HE and, with R.K. Shrestha, subsequent data treatment. We are also grateful to P. Torelli and G. Ricchiardi for their support during the measurements at APE-HE, as well as insightful discussions and advices. The authors acknowledge the CERIC-ERIC Consortium for the access to Near Ambient Pressure XPS@Charles University in Prague and financial support. Finally, we acknowledge HZB for the allocation of synchrotron radiation beamtime and BESSY Synchrotron staff for the collaboration during the experiments.

6 References

[1] P. Jing, X. Gong, B. Liu, J. Zhang, Recent advances in synergistic effect promoted catalysts for preferential oxidation of carbon monoxide, Catal. Sci. Technol. 10 (2020) 919–934. doi:10.1039/c9cy02073j.

[2] D.I. Potemkin, E.Y. Filatov, A. V. Zadesenets, A.M. Gorlova, N.A. Nikitina, D.A. Pichugina, A comparative study of CO preferential oxidation over Pt and Pt0.5Co0.5 nanoparticles: Kinetic study and quantum-chemical calculations, Mater. Lett. 260 (2020) 126915. doi:10.1016/j.matlet.2019.126915.

[3] L. Cao, W. Liu, Q. Luo, R. Yin, B. Wang, J. Weissenrieder, M. Soldemo, H. Yan, Y. Lin, Z. Sun, C. Ma, W. Zhang, S. Chen, H. Wang, Q. Guan, T. Yao, S. Wei, J. Yang, J. Lu, Atomically dispersed iron hydroxide anchored on Pt for preferential oxidation of CO in H2, Nature. 565 (2019) 631–635. doi:10.1038/s41586-018-0869-5.

[4] N. Bion, F. Epron, M. Moreno, F. Mariño, D. Duprez, Preferential oxidation of carbon monoxide in the

presence of hydrogen (PROX) over noble metals and transition metal oxides: Advantages and drawbacks, Top. Catal. 51 (2008) 76–88. doi:10.1007/s11244-008-9116-x.

[5] Y.H. Kim, S.D. Yim, E.D. Park, Selective CO oxidation in a hydrogen-rich stream over Ru/SiO 2, Catal. Today. 185 (2012) 143–150. doi:10.1016/j.cattod.2011.07.022.

[6] B. Qiao, J. Liu, Y.G. Wang, Q. Lin, X. Liu, A. Wang, J. Li, T. Zhang, J. Liu, Highly Efficient Catalysis of Preferential Oxidation of CO in H2-Rich Stream by Gold Single-Atom Catalysts, ACS Catal. 5 (2015) 6249–6254. doi:10.1021/acscatal.5b01114.

[7] K. Liu, A. Wang, T. Zhang, Recent Advances in Preferential Oxidation of CO Reaction over Platinum Group Metal Catalysts, ACS Catal. 2 (2012) 1165–1178. doi:10.1021/cs200418w.

[8] Y. Chen, J. Lin, L. Li, X. Pan, X. Wang, T. Zhang, Local structure of Pt species dictates remarkable performance on Pt/Al2O3 for preferential oxidation of CO in H2, Appl. Catal. B Environ. 282 (2021) 119588. doi:10.1016/j.apcatb.2020.119588.

[9] C. Zlotea, Y. Oumellal, K. Provost, F. Morfin, L. Piccolo, Role of hydrogen absorption in supported Pd nanocatalysts during CO-PROX: Insights from operando X-ray absorption spectroscopy, Appl. Catal. B Environ. 237 (2018) 1059–1065. doi:10.1016/j.apcatb.2018.06.059.

[10] S.S. Maluf, E.M. Assaf, CO preferential oxidation (CO-PROx) on La1 - XCe xNiO3 perovskites, Catal. Commun. 12 (2011) 703–706. doi:10.1016/j.catcom.2010.12.022.

[11] J. Ding, L. Li, H. Li, S. Chen, S. Fang, T. Feng, G. Li, Optimum Preferential Oxidation Performance of CeO2-CuOx-RGO Composites through Interfacial Regulation, ACS Appl. Mater. Interfaces. 10 (2018) 7935–7945. doi:10.1021/acsami.7b15549.

[12] A. Elmhamdi, R. Castañeda, A. Kubacka, L. Pascual, K. Nahdi, A. Martínez-Arias, Characterization and catalytic properties of CuO/CeO2/MgAl2O4for preferential oxidation of CO in H2-rich streams, Appl. Catal. B Environ. 188 (2016) 292–304. doi:10.1016/j.apcatb.2016.02.011.

[13] Y. Teng, H. Sakurai, A. Ueda, T. Kobayashi, Oxidative removal of co contained in hydrogen by using metal oxide catalysts, Int. J. Hydrogen Energy. 24 (1999) 355–358. doi:https://doi.org/10.1016/S0360-3199(98)00083-4.

[14] C.S. Polster, H. Nair, C.D. Baertsch, Study of active sites and mechanism responsible for highly selective CO oxidation in H2 rich atmospheres on a mixed Cu and Ce oxide catalyst, J. Catal. 266 (2009) 308–319. doi:10.1016/j.jcat.2009.06.021.

[15] Y. Yoshida, Y. Izumi, Recent Advances in the Preferential Thermal-/Photo-Oxidation of Carbon Monoxide: Noble Versus Inexpensive Metals and Their Reaction Mechanisms, Catal. Surv. from Asia. 20 (2016) 141–166. doi:10.1007/s10563-016-9216-8.

[16] C. Tang, J. Sun, X. Yao, Y. Cao, L. Liu, C. Ge, F. Gao, L. Dong, Efficient fabrication of active CuO-CeO2/SBA-15 catalysts for preferential oxidation of CO by solid state impregnation, Appl. Catal. B Environ. 146 (2014) 201–212. doi:10.1016/j.apcatb.2013.05.060.

[17] A. Davó-Quiñonero, I. Such-Basáñez, J. Juan-Juan, D. Lozano-Castelló, P. Stelmachowski, G. Grzybek, A. Kotarba, A. Bueno-López, New insights into the role of active copper species in CuO/Cryptomelane catalysts for the CO-PROX reaction, Appl. Catal. B Environ. 267 (2020) 118372. doi:10.1016/j.apcatb.2019.118372.

[18] O. Marie, X. Portier, N. Korsunska, L. Khomenkova, CO–PROX reactions on copper Y2O3-ZrO2 catalysts prepared by a single step co-precipitation technique, Appl. Catal. B Environ. 278 (2020) 119258. doi:10.1016/j.apcatb.2020.119258.

[19] A. Davó-Quiñonero, M. Navlani-García, D. Lozano-Castelló, A. Bueno-López, J.A. Anderson, Role of Hydroxyl Groups in the Preferential Oxidation of CO over Copper Oxide-Cerium Oxide Catalysts, ACS Catal. 6 (2016) 1723–1731. doi:10.1021/acscatal.5b02741.

[20] J.S. Elias, N. Artrith, M. Bugnet, L. Giordano, G.A. Botton, A.M. Kolpak, Y. Shao-Horn, Elucidating the Nature of the Active Phase in Copper/Ceria Catalysts for CO Oxidation, ACS Catal. 6 (2016) 1675–1679. doi:10.1021/acscatal.5b02666.

[21] A. Davó-Quiñonero, A. Davó-Quiñonero, A. Davó-Quiñonero, E. Bailón-García, S. López-Rodríguez, J. Juan-Juan, D. Lozano-Castelló, M. García-Melchor, F.C. Herrera, F.C. Herrera, E. Pellegrin, C. Escudero, A. Bueno-López, A. Bueno-López, Insights into the Oxygen Vacancy Filling Mechanism in CuO/CeO2 Catalysts:

A Key Step Toward High Selectivity in Preferential CO Oxidation, ACS Catal. 10 (2020) 6532–6545. doi:10.1021/acscatal.0c00648.

[22] X. Xie, Y. Li, Z.Q. Liu, M. Haruta, W. Shen, Low-temperature oxidation of CO catalysed by Co3O4 nanorods, Nature. 458 (2009) 746–749. doi:10.1038/nature07877.

[23] M. Khasu, T. Nyathi, D.J. Morgan, G.J. Hutchings, M. Claeys, N. Fischer, Co3O4 morphology in the preferential oxidation of CO, Catal. Sci. Technol. 7 (2017) 4806–4817. doi:10.1039/c7cy01194f.

[24] Z. Zhao, M.M. Yung, U.S. Ozkan, Effect of support on the preferential oxidation of CO over cobalt catalysts, Catal. Commun. 9 (2008) 1465–1471. doi:10.1016/j.catcom.2007.12.013.

[25] Z. Zhao, X. Lin, R. Jin, Y. Dai, G. Wang, High catalytic activity in CO PROX reaction of low cobalt-oxide loading catalysts supported on nano-particulate CeO2-ZrO2 oxides, Catal. Commun. 12 (2011) 1448–1451. doi:10.1016/j.catcom.2011.05.031.

[26] T.M. Nyathi, N. Fischer, A.P.E. York, D.J. Morgan, G.J. Hutchings, E.K. Gibson, P.P. Wells, C.R.A. Catlow, M. Claeys, Impact of Nanoparticle-Support Interactions in Co3O4/Al2O3 Catalysts for the Preferential Oxidation of Carbon Monoxide, ACS Catal. 9 (2019) 7166–7178. doi:10.1021/acscatal.9b00685.

[27] I. Czekaj, J. Wambach, O. Kröcher, Modelling Catalyst Surfaces Using DFT Cluster Calculations, (2009) 4310–4329. doi:10.3390/ijms10104310.

[28] Z. Zhao, R. Jin, T. Bao, X. Lin, G. Wang, Mesoporous ceria-zirconia supported cobalt oxide catalysts for CO preferential oxidation reaction in excess H2, Appl. Catal. B Environ. 110 (2011) 154–163. doi:10.1016/j.apcatb.2011.08.038.

[29] L.E. Gómez, I.S. Tiscornia, A. V. Boix, E.E. Miró, Co/ZrO2 catalysts coated on cordierite monoliths for CO preferential oxidation, Appl. Catal. A Gen. 401 (2011) 124–133. doi:10.1016/j.apcata.2011.05.007.

[30] T. Nyathi, N. Fischer, A.P.E. York, M. Claeys, Environment-Dependent Catalytic Performance and Phase Stability of Co3O4 in the Preferential Oxidation of Carbon Monoxide Studied In Situ, ACS Catal. 10 (2020) 11892–11911. doi:10.1021/acscatal.0c02653.

[31] L. Ma, C.Y. Seo, X. Chen, K. Sun, J.W. Schwank, Indium-doped Co3O4nanorods for catalytic oxidation of CO and C3H6towards diesel exhaust, Appl. Catal. B Environ. 222 (2018) 44–58. doi:10.1016/j.apcatb.2017.10.001.

[32] Q. Zhang, X. Liu, W. Fan, Y. Wang, Manganese-promoted cobalt oxide as efficient and stable non-noble metal catalyst for preferential oxidation of CO in H2 stream, Appl. Catal. B Environ. 102 (2011) 207–214. doi:10.1016/j.apcatb.2010.11.043.

[33] Z. Zhao, T. Bao, Y. Zeng, G. Wang, T. Muhammad, Efficient cobalt-manganese oxide catalyst deposited on modified AC with unprecedented catalytic performance in CO preferential oxidation, Catal. Commun. 32 (2013) 47–51. doi:10.1016/j.catcom.2012.12.001.

[34] Z. Zhao, X. Lin, R. Jin, G. Wang, T. Muhammad, MO x (M=Mn, Fe, Ni or Cr) improved supported Co 3O 4 catalysts on ceria-zirconia nanoparticulate for CO preferential oxidation in H 2-rich gases, Appl. Catal. B Environ. 115–116 (2012) 53–62. doi:10.1016/j.apcatb.2011.12.001.

[35] T. Bao, Z. Zhao, Y. Dai, X. Lin, R. Jin, G. Wang, T. Muhammad, Supported Co3O4-CeO2 catalysts on modified activated carbon for CO preferential oxidation in H2-rich gases, Appl. Catal. B Environ. 119–120 (2012) 62–73. doi:10.1016/j.apcatb.2012.02.018.

[36] L.E. Gómez, A. V. Boix, E.E. Miró, Co/ZrO2, Co/CeO2and MnCoCe structured catalysts for COPrOx, Catal. Today. 216 (2013) 246–253. doi:10.1016/j.cattod.2013.05.010.

[37] Z. Zhao, R. Jin, Y. Li, Y. Dai, T. Muhammad, Mesostructured Co-Ce-Zr-Mn-O composite as a potential catalyst for efficient removal of carbon monoxide from hydrogen-rich stream, Catal. Sci. Technol. 3 (2013) 2130–2139. doi:10.1039/c3cy00154g.

[38] L.E. Gómez, E.E. Miró, A. V. Boix, Spectroscopic characterization of Mn-Co-Ce mixed oxides, active catalysts for COPROX reaction, Int. J. Hydrogen Energy. 38 (2013) 5645–5654. doi:10.1016/j.ijhydene.2013.03.004.

[39] M.T. Le, T.T. Nguyen, P.T.M. Pham, E. Bruneel, I. Van Driessche, Activated MnO2-Co3O4-CeO2 catalysts for the treatment of CO at room temperature, Appl. Catal. A Gen. 480 (2014) 34–41. doi:10.1016/j.apcata.2014.04.034.

[40] J.E. Park, E.D. Park, Effects of surface area of Co-Mn-O catalysts on the selective CO oxidation in H2, Catal. Letters. 144 (2014) 607–614. doi:10.1007/s10562-013-1185-1.

[41] L. Lukashuk, K. Föttinger, E. Kolar, C. Rameshan, D. Teschner, M. Hävecker, A. Knop-Gericke, N. Yigit, H. Li, E. McDermott, M. Stöger-Pollach, G. Rupprechter, Operando XAS and NAP-XPS studies of preferential CO oxidation on Co3O4 and CeO2-Co3O4 catalysts, J. Catal. 344 (2016) 1–15. doi:10.1016/j.jcat.2016.09.002.

[42] W.Y. Hernández, M.A. Centeno, F. Romero-Sarria, S. Ivanova, M. Montes, J.A. Odriozola, Modified cryptomelane-type manganese dioxide nanomaterials for preferential oxidation of CO in the presence of hydrogen, in: Catal. Today, Elsevier, 2010: pp. 160–165. doi:10.1016/j.cattod.2010.03.010.

[43] Z. Zhao, R. Jin, T. Bao, H. Yang, X. Lin, G. Wang, Mesoporous Ce x Mn 1-x O 2 composites as novel alternative carriers of supported Co 3 O 4 catalysts for CO preferential oxidation in H 2 stream, Int. J. Hydrogen Energy. 37 (2012) 4774–4786. doi:10.1016/j.ijhydene.2011.12.057.

[44] J.A. Gómez-Cuaspud, M. Schmal, Nanostructured metal oxides obtained by means polymerization-combustion at low temperature for CO selective oxidation, Int. J. Hydrogen Energy. 38 (2013) 7458–7468. doi:10.1016/j.ijhydene.2013.04.024.

[45] Q. Guo, S. Chen, Y. Liu, Y. Wang, Stability of Co-Ce-Mn mixed-oxide catalysts for CO preferential oxidation in H2-rich gases, Chem. Eng. J. 165 (2010) 846–850. doi:10.1016/j.cej.2010.10.029.

[46] Q. Guo, Y. Liu, MnOx modified Co3O4-CeO2 catalysts for the preferential oxidation of CO in H2-rich gases, Appl. Catal. B Environ. 82 (2008) 19–26. doi:10.1016/j.apcatb.2008.01.007.

[47] Z. Zhao, Y. Li, T. Bao, G. Wang, T. Muhammad, Hierarchically nanoporous Co-Mn-O/FeOxas a high performance catalyst for CO preferential oxidation in H2-rich stream, Catal. Commun. 46 (2014) 28–31. doi:10.1016/j.catcom.2013.11.019.

[48] L. Zhong, T. Kropp, W. Baaziz, O. Ersen, D. Teschner, R. Schlögl, M. Mavrikakis, S. Zafeiratos, Correlation between Reactivity and Oxidation State of Cobalt Oxide Catalysts for CO Preferential Oxidation, ACS Catal. 9 (2019) 8325–8336. doi:10.1021/acscatal.9b02582.

[49] L. Michel, S. Sall, T. Dintzer, C. Robert, A. Demange, V. Caps, Graphene-supported 2D cobalt oxides for catalytic applications, Faraday Discuss. (2020). doi:10.1039/c9fd00110g.

[50] K. Frey, V. Iablokov, G. Sáfrán, J. Osán, I. Sajó, R. Szukiewicz, S. Chenakin, N. Kruse, Nanostructured MnOx as highly active catalyst for CO oxidation, J. Catal. 287 (2012) 30–36. doi:10.1016/j.jcat.2011.11.014.

[51] K. Ramesh, L. Chen, F. Chen, Y. Liu, Z. Wang, Y.F. Han, Re-investigating the CO oxidation mechanism over unsupported MnO, Mn2O3 and MnO2 catalysts, Catal. Today. 131 (2008) 477–482. doi:10.1016/j.cattod.2007.10.061.

[52] L.C. Wang, Q. Liu, X.S. Huang, Y.M. Liu, Y. Cao, K.N. Fan, Gold nanoparticles supported on manganese oxides for low-temperature CO oxidation, Appl. Catal. B Environ. 88 (2009) 204–212. doi:10.1016/j.apcatb.2008.09.031.

[53] F. Besenbacher, I. Chorkendorff, B.S. Clausen, B. Hammer, A.M. Molenbroek, J.K. Nørskov, I. Stensgaard, Design of a surface alloy catalyst for steam reforming, Science (80-.). 279 (1998) 1913–1915. doi:10.1126/science.279.5358.1913.

[54] W. Huang, Oxide Nanocrystal Model Catalysts, Acc. Chem. Res. 49 (2016) 520–527. doi:10.1021/acs.accounts.5b00537.

[55] G. Couvret, G. Genay, C. Robert, L. Michel, V. Caps, Intercalation of Copper Phthalocyanine Within Bulk Graphite as a New Strategy Toward the Synthesis of CuO-Based CO Oxidation Catalysts, Front. Chem. 8 (2020) 735. doi:10.3389/fchem.2020.00735.

[56] A. Bishnoi, S. Kumar, N. Joshi, Chapter 9 - Wide-Angle X-ray Diffraction (WXRD): Technique for Characterization of Nanomaterials and Polymer Nanocomposites, in: S. Thomas, R. Thomas, A.K. Zachariah, R.K.B.T.-M.M. in N.C. Mishra (Eds.), Micro Nano Technol., Elsevier, 2017: pp. 313–337. doi:https://doi.org/10.1016/B978-0-323-46141-2.00009-2.

[57] R. Follath, M. Hävecker, G. Reichardt, K. Lips, J. Bahrdt, F. Schäfers, P. Schmid, The energy materials in-situ laboratory Berlin (EMIL) at BESSY II, in: J. Phys. Conf. Ser., 2013: p. 212003. doi:10.1088/1742-6596/425/21/212003.

[58] S. Hendel, F. Schäfers, M. Hävecker, G. Reichardt, M. Scheer, J. Bahrdt, K. Lips, The EMIL project at

BESSY II: Beamline design and performance, in: AIP Conf. Proc. 1741, 2016: p. 030038. doi:10.1063/1.4952861.

[59] C. Castán-Guerrero, D. Krizmancic, V. Bonanni, R. Edla, A. Deluisa, F. Salvador, G. Rossi, G. Panaccione, P. Torelli, A reaction cell for ambient pressure soft x-ray absorption spectroscopy, Rev. Sci. Instrum. 89 (2018) 054101. doi:10.1063/1.5019333.

[60] D.H. Simonne, A. Martini, M. Signorile, A. Piovano, L. Braglia, P. Torelli, E. Borfecchia, G. Ricchiardi, THORONDOR : a software for fast treatment and analysis of low-energy XAS data, J. Synchrotron Radiat. 27 (2020) 1741–1752. doi:10.1107/s1600577520011388.

[61] B. Gilbert, B.H. Frazer, A. Belz, P.G. Conrad, K.H. Nealson, D. Haskel, J.C. Lang, G. Srajer, G. De Stasio, Multiple scattering calculations of bonding and X-ray absorption spectroscopy of manganese oxides, J. Phys. Chem. A. 107 (2003) 2839–2847. doi:10.1021/jp021493s.

[62] B. Ravel, M. Newville, ATHENA, ARTEMIS, HEPHAESTUS: data analysis for X-ray absorption spectroscopy using IFEFFIT, J. Synchrotron Rad. 12 (2005) 537–541.

[63] L. Zhong, S. Zafeiratos, Correlation of the reactants flow with the surface state of cobalt catalysts under COPrOx reaction conditions, n.d. doi:in prearation.

[64] E.S. Ilton, J.E. Post, P.J. Heaney, F.T. Ling, S.N. Kerisit, XPS determination of Mn oxidation states in Mn (hydr)oxides, Appl. Surf. Sci. 366 (2016) 475–485. doi:10.1016/j.apsusc.2015.12.159.

[65] D.E. Parry, Atomic calculation of photoionization cross-sections and asymmetry parameters J.-J. YEH, Rapid Commun. Mass Spectrom. 8 (1994) 579.

[66] W. Smekal, W.S.M. Werner, C.J. Powell, Simulation of electron spectra for surface analysis (SESSA): A novel software tool for quantitative Auger-electron spectroscopy and X-ray photoelectron spectroscopy, Surf. Interface Anal. 37 (2005) 1059–1067. doi:10.1002/sia.2097.

[67] Q. Cheng, Y. Tian, S. Lyu, N. Zhao, K. Ma, T. Ding, Z. Jiang, L. Wang, J. Zhang, L. Zheng, F. Gao, L. Dong, N. Tsubaki, X. Li, Confined small-sized cobalt catalysts stimulate carbon-chain growth reversely by modifying ASF law of Fischer–Tropsch synthesis, Nat. Commun. 9 (2018). doi:10.1038/s41467-018-05755-8.

[68] O.A. Bulavchenko, E.Y. Gerasimov, T.N. Afonasenko, Reduction of double manganese-cobalt oxides:: In situ XRD and TPR study, Dalt. Trans. 47 (2018) 17153–17159. doi:10.1039/c8dt04137g.

[69] T.E. Feltes, L. Espinosa-Alonso, E. de Smit, L. D'Souza, R.J. Meyer, B.M. Weckhuysen, J.R. Regalbuto, Selective adsorption of manganese onto cobalt for optimized Mn/Co/TiO2 Fischer-Tropsch catalysts, J. Catal. 270 (2010) 95–102. doi:10.1016/j.jcat.2009.12.012.

[70] R. Yang, Z. Xia, Z. Zhao, F. Sun, X. Du, H. Yu, S. Gu, L. Zhong, J. Zhao, Y. Ding, Z. Jiang, Characterization of CoMn catalyst by in situ X-ray absorption spectroscopy and wavelet analysis for Fischer–Tropsch to olefins reaction, J. Energy Chem. 32 (2019) 118–123. doi:10.1016/j.jechem.2018.07.005.

[71] W. Han, F. Dong, W. Han, Z. Tang, Fabrication of homogeneous and highly dispersed CoMn catalysts for outstanding low temperature catalytic oxidation performance, New J. Chem. 43 (2019) 12846–12857. doi:10.1039/c9nj03450a.

[72] Y. V. Golikov, S.Y. Tubin, V.P. Barkhatov, V.F. Balakirev, Phase diagrams of the CoMnO system in air, J. Phys. Chem. Solids. 46 (1985) 539–544. doi:10.1016/0022-3697(85)90215-X.

[73] E. Rios, J.L. Gautier, G. Poillerat, P. Chartier, Mixed valency spinel oxides of transition metals and electrocatalysis: Case of the MnxCo3-xO4 system, Electrochim. Acta. 44 (1998) 1491–1497. doi:10.1016/S0013-4686(98)00272-2.

[74] F. Morales, D. Grandjean, A. Mens, F.M.F. De Groot, B.M. Weckhuysen, X-ray absorption spectroscopy of Mn/Co/TiO2 fischer-tropsch catalysts: Relationships between preparation method, molecular structure, and catalyst performance, J. Phys. Chem. B. 110 (2006) 8626–8639. doi:10.1021/jp0565958.

[75] J.M.J. Mateos, J. Morales, J.L. Tirado, Cation-deficient Mn, Co spinel oxides obtained by thermal decomposition of carbonate precursors, J. Solid State Chem. 82 (1989) 87–94. doi:10.1016/0022-4596(89)90226-0.

[76] J. Gao, Y. Wang, Y. Ping, D. Hu, G. Xu, F. Gu, F. Su, A thermodynamic analysis of methanation reactions of carbon oxides for the production of synthetic natural gas, RSC Adv. 2 (2012) 2358–2368. doi:10.1039/c2ra00632d.

[77] V. Papaefthimiou, T. Dintzer, V. Dupuis, A. Tamion, F. Tournus, A. Hilion, D. Teschner, M. Hävecker, A. Knop-Gericke, R. Schlögl, S. Zafeiratos, A. Hillion, D. Teschner, M. Hävecker, A. Knop-Gericke, R. Schlögl, S. Zafeiratos, Nontrivial redox behavior of nanosized cobalt: New insights from ambient pressure X-ray photoelectron and absorption spectroscopies, ACS Nano. 5 (2011) 2182–2190. doi:10.1021/nn103392x.

[78] T.M. Nyathi, N. Fischer, A.P.E. York, M. Claeys, Effect of crystallite size on the performance and phase transformation of Co3O4/Al2O3 catalysts during CO-PrOx-an: In situ study, Faraday Discuss. 197 (2017) 269–285. doi:10.1039/c6fd00217j.

[79] M.C. Biesinger, B.P. Payne, A.P. Grosvenor, L.W.M. Lau, A.R. Gerson, R.S.C. Smart, Resolving surface chemical states in XPS analysis of first row transition metals, oxides and hydroxides: Cr, Mn, Fe, Co and Ni, Appl. Surf. Sci. 257 (2011) 2717–2730. doi:10.1016/j.apsusc.2010.10.051.

[80] V. Di Castro, G. Polzonetti, XPS study of MnO oxidation, J. Electron Spectros. Relat. Phenomena. 48 (1989) 117–123. doi:10.1016/0368-2048(89)80009-X.

[81] H.W. Nesbitt, D. Banerjee, Interpretation of XPS Mn(2p) spectra of Mn oxyhydroxides and constraints on the mechanism of MnO2 precipitation, Am. Mineral. 83 (1998) 305–315. doi:10.2138/am-1998-3-414.

[82] I. Nakamura, M. Haneda, H. Hamada, T. Fujitani, Direct decomposition of nitrogen monoxide over a K-deposited Co(0 0 0 1) surface: Comparison to K-doped cobalt oxide catalysts, J. Electron Spectros. Relat. Phenomena. 150 (2006) 150–154. doi:10.1016/j.elspec.2005.01.295.

[83] S. Turczyniak, W. Luo, V. Papaefthimiou, N.S. Ramgir, M. Haevecker, A. MacHocki, S. Zafeiratos, A Comparative Ambient Pressure X-ray Photoelectron and Absorption Spectroscopy Study of Various Cobalt-Based Catalysts in Reactive Atmospheres, Top. Catal. 59 (2016) 532–542. doi:10.1007/s11244-015-0531-5.

[84] O.A. Bulavchenko, T.N. Afonasenko, S.S. Sigaeva, A. V. Ivanchikova, A.A. Saraev, E.Y. Gerasimov, V. V. Kaichev, S. V. Tsybulya, The Structure of Mixed Mn–Co Oxide Catalysts for CO Oxidation, Top. Catal. 63 (2020) 75–85. doi:10.1007/s11244-020-01230-1.

[85] L. Zhong, M. Barreau, V. Caps, V. Papaefthimiou, M. Haevecker, D. Teschner, W. Baaziz, E. Borfecchia, L. Braglia, S. Zafeiratos, Improving the Catalytic Performance of Cobalt for CO Preferential Oxidation by Stabilizing the Active Phase through Vanadium Promotion, ACS Catal. 11 (2021) 5369–5385. doi:10.1021/acscatal.0c05482.

TOC

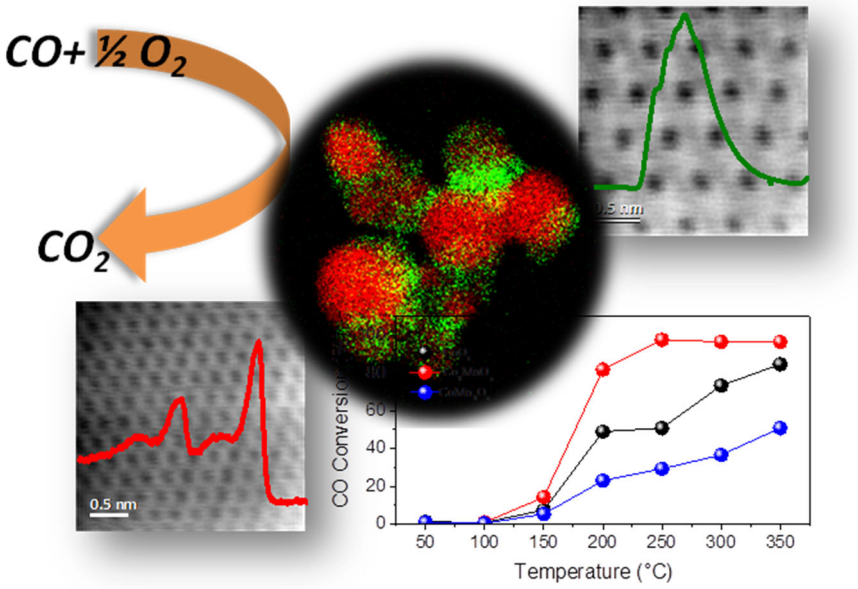
CO+ ½ O2
CO2
0.5 nm
0.5 nm
CO Conversion
60
40
20
0
50
100
150
200
250
300
350
Temperature (°C)